1986

Design of a Two-Layer, Capacitively Coupled, Microstrip Patch Antenna Element for Broadband Applications

Robert T. Cock
University of Central Florida

DESIGN OF A TWO-LAYER, CAPACITIVELY COUPLED, MICROSTRIP PATCH ANTENNA ELEMENT FOR BROADBAND APPLICATIONS

BY

ROBERT TAYLOR COCK
B.S.E.E., University of South Florida, 1981

THESIS

Submitted in partial fulfillment of the requirements
for the degree of Master of Science in Engineering
in the Graduate Studies Program of the College of Engineering
University of Central Florida
Orlando, Florida

Fall Term
1986

ABSTRACT

A broadband, contiguous stacked, two-layer, square microstrip patch antenna element design is described which can be used for linear or circular polarization. Single layer microstrip patch theory for the rectangular patch radiator is presented and used as a basis for understanding the two-layer patch configuration. The theory is modified to predict radiation patterns and resonant frequencies of the two-layer microstrip patch antenna element. Experimental results include the radiation patterns, dominant resonant frequencies (TM_{10} mode), return loss (S_{11}), and bandwidth for X band elements as a function of dielectric constants, dielectric thicknesses, and patch sizes.

ACKNOWLEDGEMENTS

The author would like to express his appreciation toward those who were patient enough to tolerate the years of his graduate studies and the months spent in preparing this paper. In particular, the author feels obliged to Dr. C. G. Christodoulou at the University of Central Florida and to Martin Marietta Aerospace in Orlando, Florida.

TABLE OF CONTENTS

LIST OF FIGURES

LIST OF TABLES

NOMENCLATURE

L = rectangular microstrip patch length

W = rectangular microstrip patch width

h = dielectric thickness or height

ϵ_r = relative permittivity (dielectric constant)

ϵ_e = effective relative permittivity

ϵ_o = permittivity of free space 8.854×10^{-12} Farads/meter

$\epsilon = \epsilon_r \epsilon_o$

μ_o = permeability of free space $4\pi \times 10^{-7}$ Henries/meter

λ_o = wavelength in free space

λ_d = wavelength in dielectric

λ_g = microstrip guide wavelength

c = speed of light in a vacuum 2.998×10^{10} cm/sec

f = frequency in hertz

k = propagation constant

$\mathbf{E}$ = electric field vector (Volts/meter)

E = electric field scalar

$\mathbf{H}$ = magnetic field vector (Amps/meter)

H = magnetic field scalar

$\mathbf{x}$ = unit vector in the X direction

$\mathbf{y}$ = unit vector in the Y direction

$\mathbf{z}$ = unit vector in the Z direction

$\mathbf{n}$ = unit vector in the normal direction

$\mathbf{D}$ = electric flux density vector (Coulombs/meter^2)

$\mathbf{M}$ = magnetic current density vector

U = radiation intensity (Watts/Steradian)

η = intrinsic impedance in free space ($120\pi\ \Omega$)

P = power (Watts)

D_o = directivity (dimensionless or dB, as noted)

G_o = gain (dimensionless or dB, as noted)

σ = conductivity

e_t = total efficiency

SECTION I

INTRODUCTION

Microstrip antennas are fast becoming a viable practical solution to the demand for low profile, low cost, conformal antennas. They have been developed over the frequency range of about 100 MHz up to about 60 GHz and are used in diverse applications including [1]:

- aircraft and spacecraft/satellite communications
- doppler and other radars
- radar altimeter
- missile telemetry
- weapon fusing
- environmental intrumentation and remote sensing
- satellite navigation receiver
- biomedical radiator, etc.

The concept of the microstrip antenna dates back to work in 1953 by Deschamps [1], which was shortly after the introduction of the microstrip transmission system. However, due mostly to material and process constraints, it was not until the 1970s that the first practical microstrip antennas were developed [1,3]. By that time, photoetching techniques had

improved and microwave materials with a wide range of dielectric constants, thicknesses, low loss tangents and good thermal and mechanical properties were available.

Microstrip patch antennas consist of a very thin conducting patch, usually of copper or gold, placed a small fraction of a wavelength above a ground plane. The patch and the ground plane are separated by a dielectric

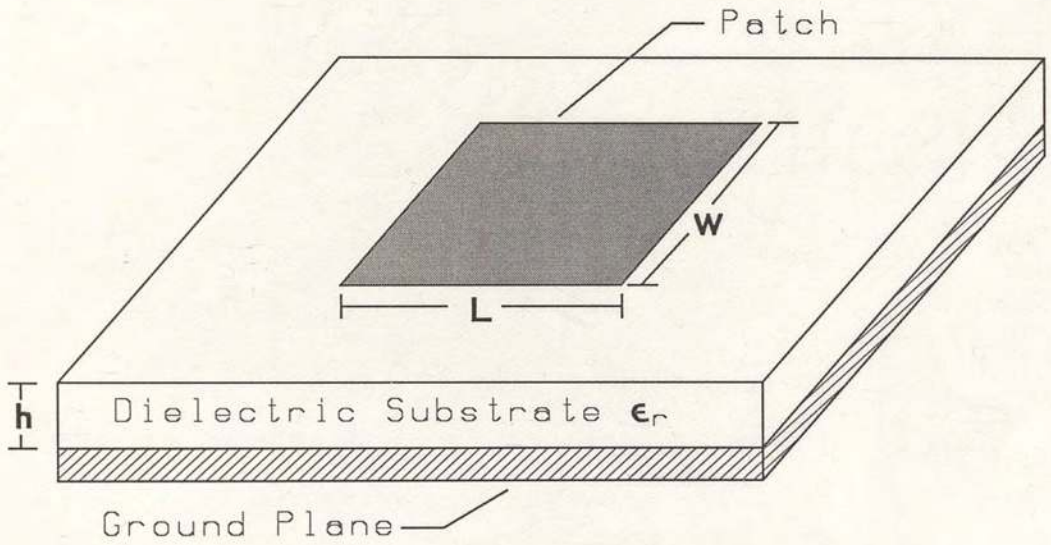

Figure 1. Rectangular Microstrip Patch Element.

slab or substrate forming a sandwich of two parallel conducting plates as shown in Figure 1. The patch becomes a radiating element when a feed voltage is applied between it and the ground plane. The dimensions of an

open circuited patch radiating element are comparable to a half wavelength of its fundamental resonance. The patches are usually photoetched on one side of a polytetrafluoroethylene (PTFE) composite microstrip dielectric substrate such as RT Duroid. Microstrip feed lines are often attached to the patch edges (feed line width<<patch width) and are photoetched with the patches [1,3]. Another common feed is a coaxial line feed where the inner coax conductor attaches to the radiating patch and the outer conductor to the ground plane [3]. The patch radiating elements are broad beamed and are generally put in arrays to obtain greater directivity. Both linear and circular polarizations are achievable. Microstrip patch radiating elements may be rectangular, circular, pentagonal or virtually any shape. However, for ease of analysis and fabrication, the most commonly used element is rectangular. The theory and applications presented in the following chapters of this work are concerned exclusively with rectangular or square elements.

Microstrip patch antenna element radiators have several advantages as compared to conventional microwave antennas including [1,2]:

- very thin, low profile, light weight planar configuration; may be easily mounted on missiles, satellites, planes, etc. and can be made conformal, not disturbing the aerodynamics of the host vehicle
- low fabrication cost; easily mass produced; compatible with printed circuit board technology and integration techniques
- can be directly placed on metal surfaces since the back is a metal ground plane
- no cavity backing required
- the antennas have low scattering cross section

- the antennas can be made with linear or circular polarization
- dual frequency antennas are possible
- feed lines to the elements and matching networks are fabricated simultaneously with the antenna structure
- microstrip antennas can be used in modular or active element designs where solid state devices such as amplifiers, phase shifters, etc. are integrated directly with the antenna substrate

However, standard microstrip patch antennas also have several disadvantages including:

- an inherent narrow bandwidth on the order of 1 to 5% (2:1 VSWR)
- higher losses and thus somewhat lower gain than other conventional microwave and millimeter wave antennas
- poor isolation between the feeds and the radiating elements
- extraneous radiation from feeds, junctions and surface waves
- lower power handling capability

Much investigation toward the correction of these disadvantages is now underway. The body of this work is dedicated to improving the bandwith of microstrip radiators. A practical design capable of greater than 20% bandwidth for a 2:1 VSWR is presented.

SECTION II

TWO-LAYER MICROSTRIP PATCH ANTENNA ELEMENT

A two-layer microstrip patch design is proposed here as a solution to the inherent narrow bandwidth of the standard single layer microstrip patch radiator. The design makes use of a contiguous two-layer configuration and is accomplished with only minor increases in substrate height and element complexity as compared to the standard microstrip antenna element shown in Figure 1. The standard single patch element is a strongly resonant device. In frequency response, it resembles a parallel R L C circuit with high Q,

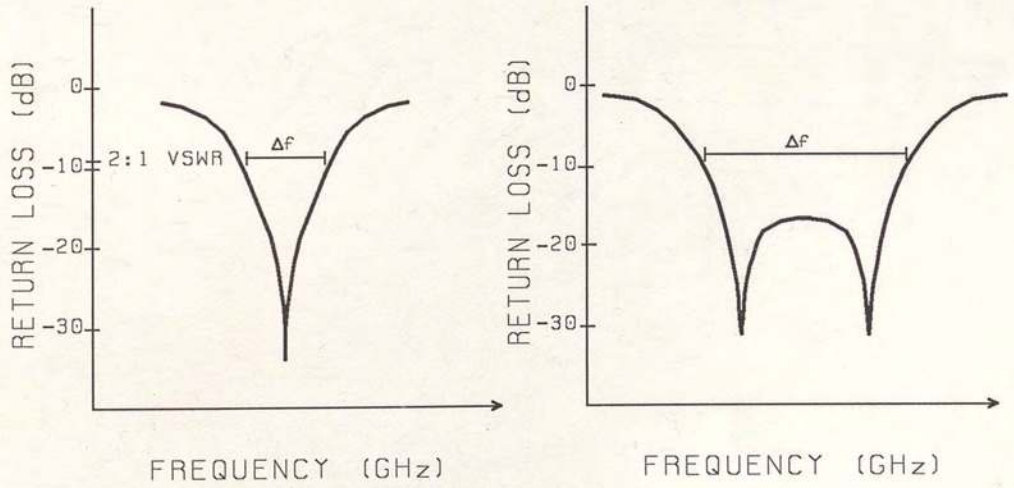

Figure 2. Typical Return Loss of a Standard Resonant Microstrip Patch Element (Left); Desired Dual Resonant Return Loss (Right).

and thus narrow bandwidth. The idea proposed is to increase this bandwidth by creating a design with two closely tuned resonances as opposed to the one resonance of the standard patch element. Even though each resonance will still be sharp (high Q), together they can cover a frequency band Δf much broader than a single resonance element. A comparison of expected return loss responses is shown in Figure 2. In order to accomplish this dual resonance, two patches are used in each element. The patches are assembled in the two-layer design configuration shown in Figure 3.

The patches in this two-layer design are used as open circuit microstrip half wave resonators. The lower patch is the feed patch and is etched a short distance h_L above a ground plane ($h_L << \lambda$) on one side of a high dielectric substrate with relative permittivity ϵ_{rLower} (ϵ_{rL} on the order of 10). When using the element in an array, feed structures and other passive and active circuits will be integrated along with the lower feed patches on this high dielectric. Since feed and patch structure dimensions are relative to wavelength (λ_d) in the dielectric, and since

$$\lambda_d = (c \; / \sqrt{\epsilon_r}) \; / f \qquad (2-1)$$

where c is the speed of light in a vacuum and f is the frequency in hertz, then the high dielectric allows more space for the feed structures and patches. The lower patch is edge fed from the source. Feeding can be at

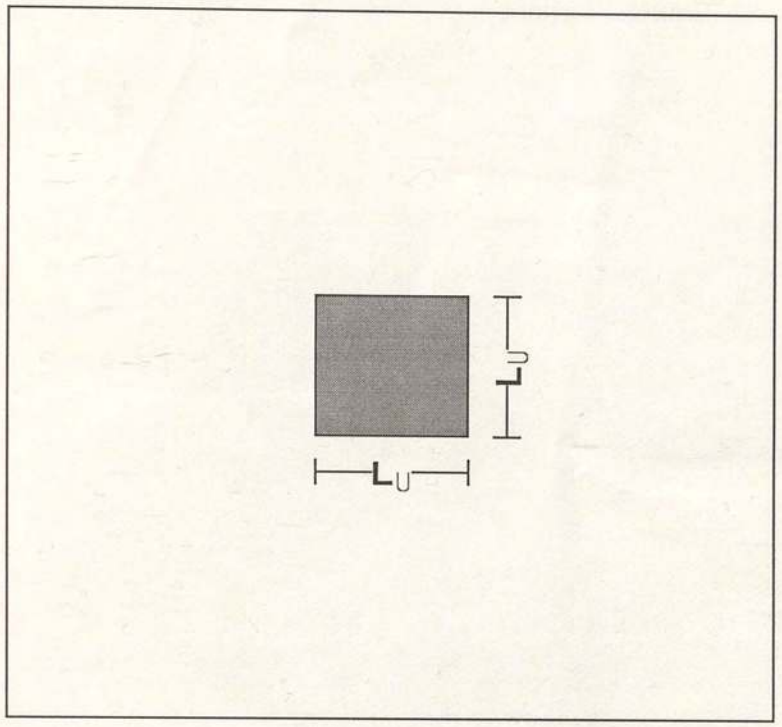

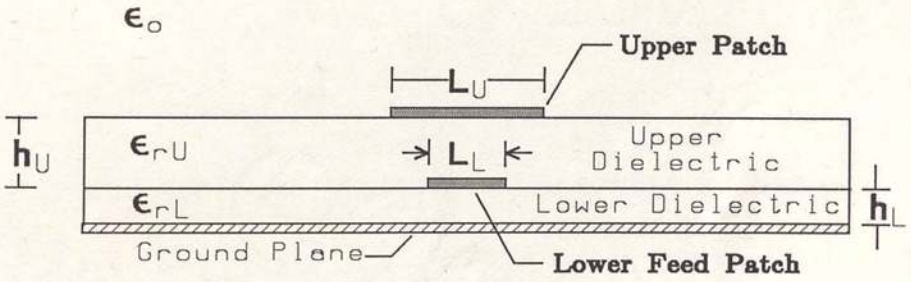

Figure 3. Two–Layer Microstrip Patch Antenna Element.

one edge for linear polarization or two perpendicular edges can be fed with the same amplitude and 90° phase difference for circular polarization. The upper patch of the element is etched on a low dielectric substrate with relative permittivity ϵ_{rUpper} (ϵ_{rU} on the order of 2). This low dielectric means that the upper patch must be larger than the lower patch to maintain similar frequencies of dominant resonance. A low dielectric, as used for the upper patch layer, is known to yield a more efficient radiator. The relative permeability of the substrate materials used in the microstrip patch design is assumed to be 1 ($\mu_r = 1$).

The upper patch is parasitically or capacitively (electromagnetically) coupled to the feed patch. No physical connection is made to the upper patch. The patches are symmetrical in shape, being square, and symmetrical in position, aligned with their centers on an axis normal to the substrate in the broadside direction and with their edges parallel. The symmetry allows use of the design for either linear or circular polarizations. The stacking localizes radiation across the useful band of the element to a small source area in space, which makes array use of the element easier. The patch layers are contiguous with no air gap in between. This is an important asset when a launch-hardened antenna is needed to overcome high G (gravitational) forces such as at the firing of a guided projectile or missile. The contiguous design also yields an antenna easier to manufacture than an air gap

configuration. Table 1 contains an overview of the features of the proposed two-layer design.

TABLE 1.

TWO-LAYER MICROSTRIP PATCH ANTENNA ELEMENT DESIGN FEATURES

FEATURE	RESULT
• Two closely tuned resonances	• Allows bandwidths > 20% (2:1 VSWR)
• Highly symmetrical	• The design can be used for linear or circular polarization applications
• Contiguous stacking; no air gap between elements	• Yields an easier to manufacture and launch-harden element
• Lower feed etched on high dielectric	• Lends itself to integration with feed and other passive and active devices
• Small element architecture	• Easily used in an array

The broadbanding method consists of detuning the upper and lower patch resonant frequencies of the two-layer design in opposite directions away from the desired center frequency. At the same time, an input match necessary to obtain a VSWR less than the specified maximum must be maintained across the band. The usable band of frequencies or bandwidth of the element is between frequencies where the VSWR is equal to the specified maximum. In this paper, the VSWR specification in bandwidth calculations is taken to be 2:1 (-9.54dB return loss). Looking at the typical return loss data of Figure 2, the bandwidth (BW) is calculated as:

$$\text{BW}\ (\%) = [\Delta f / (\text{center frequency } f_c)] \times 100 \qquad (2\text{-}2)$$

As mentioned previously, bandwidth of the standard single layer patch element is ≈1 to 5%, while experimental results show that the two-layer design is capable of greater than 20% bandwidths.

It is obvious that the two patches in the proposed design will be coupled, each affecting the resonant frequency and input impedance of the other. However, dominant or first-order effects on the element behavior are from dielectric constants and patch sizes. Thus, some approximations to element behavior can be made by isolating the individual patch elements. Second-order effects include coupling, dielectric thicknesses and resultant effective dielectric constants caused by fields being contained in more than one permittivity. These effects must be accounted for, before accurate predictions can be made.

Other attempts at broadbanding microstrip antennas have been reported in the literature. Descriptions of some of these, along with some of their disadvantages, are given in Appendix A.

SECTION III

THEORETICAL INVESTIGATION OF MICROSTRIP PATCH RADIATORS

Several models have been proposed to theoretically predict the behavior (radiation pattern, directivity, gain, efficiency, input impedance, resonant frequency, etc.) of the microstrip patch radiator. Two of these models which give some accurate results and good insight with reasonable mathematical rigor are the transmission line and the transverse magnetic (TM) cavity resonator model [1–7]. It is apparent that these models are reasonable since the microstrip patch antenna is actually a piece of a microstrip transmission system as well as a dielectric filled cavity (bounded on top and bottom by the patch and ground plane conductors and on the sides by an open circuit simulated by a magnetic wall). A look at the radiation mechanism of the microstrip patch element will give further insight into the patch behavior and use of these models.

Radiation Mechanism

The close proximity of the conducting layers indicates that between the patch and the ground plane, the electric (**E**) field exists only in the **z** direction [5], as shown in Figure 4(c). At the radiating edges of the patch,

E field fringes escape through the "leaky" magnetic walls of the open circuit. These open circuit edges are thin slot or aperture radiators, being formed by the edge of the microstrip patch and the ground plane directly beneath. The dimension of the slot is h by W (W = L for square patch). Since these apertures are very narrow ($h << \lambda$), and are above a ground plane, they radiate nearly uniformly into the half space above the ground plane [7]. The radiation edges are the feed edge and its opposite (the two ends of the

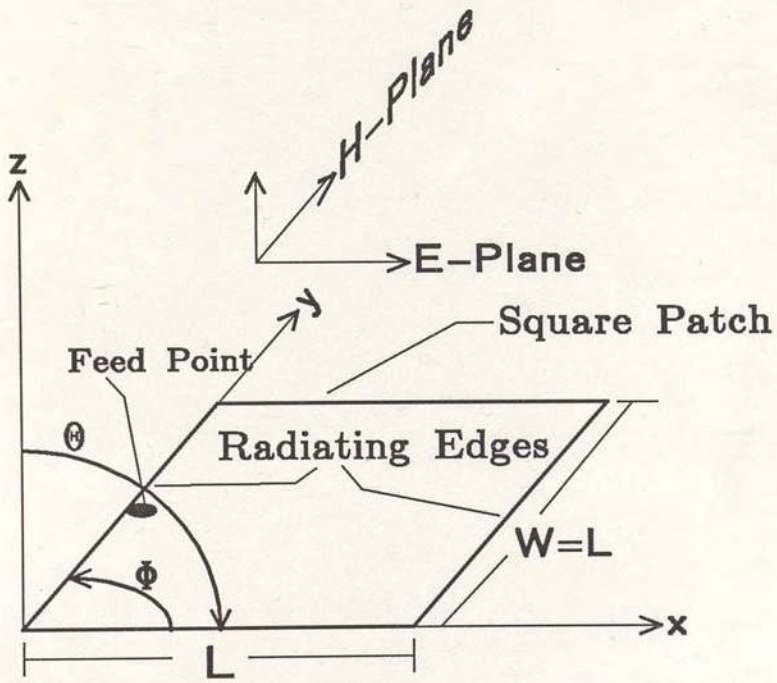

a) Coordinate System for Patch.

Figure 4(a). Microstrip Patch Antenna Element.

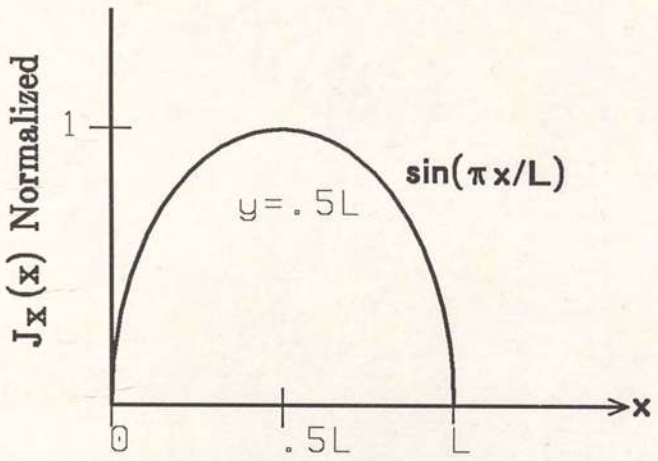

b) Approximate Current Distribution as a Function of x, Using Dyadic Green's Function Analysis [16].
($J_x(y)$ is nearly uniform. J_y is negligible.)

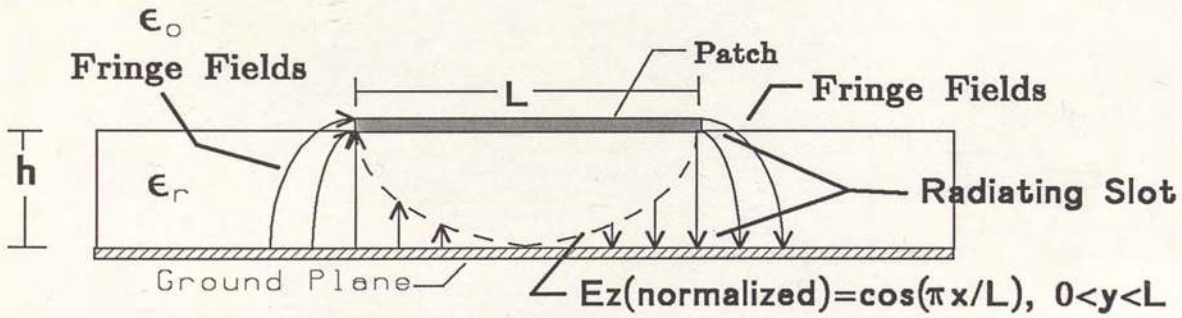

c) Element Cross Section Showing Electric Field Distribution for the Fundamental Resonance (TM_{10}) Mode Using the Cavity Model (Variations with h and W negligible).

Figure 4(b) and (c). Microstrip Patch Antenna Element.

resonant standing wave). The two slots form a two element array. The spacing between the slots is $L \approx \lambda_g/2 \approx \lambda_d/2$, since the patch is an open circuit half wave resonator, where λ_d is the wave length in the dielectric ($\lambda_d = \lambda_o/(\epsilon_r)^{1/2}$) and λ_g is the wavelength in a microstrip line. Due to this spacing the slots are excited 180° out of phase as shown in Figure 4(c). Since the slots are also spaced approximately, but less than, 180° apart relative to λ_o, the far field radiation normal to the element adds constructively, while tangential (end fire) radiation cancels, making the patch element a broadside radiator. The external **E** field and therefore the radiation intensity pattern of the microstrip patch antenna element can now be found by determining the pattern of the aperture radiator and multiplying it by the two element array pattern of the two slots [4].

$$[\text{Total Pattern}] = [\text{Element Factor}]\,[\text{Array Factor}] \qquad (3\text{–}1)$$

Each aperture radiates as a magnetic dipole with magnetic current density **M** [1,4]:

$$\mathbf{M} = -2\mathbf{n} \times \mathbf{E}_{aperture} \qquad (3\text{–}2)$$
$$= 2(V_o/h)\,\mathbf{y} \quad \text{for the coordinates of Figure 4(a)}$$
$$= 2(V_o/h)\,\mathbf{z} \quad \text{for the coordinates of Figure 5}$$

where $\mathbf{E}_{aperture}$ = (feed voltage V_o)/(dielectric height h); **n**, **y**, and **z** are unit vectors in the normal, y and z directions respectively (**n** is normal to the

aperture of the slot). For the coordinate system of Figure 5 (these coordinates produce a simpler expression), the far field* expressions for **E** and **H** are [4] (time harmonic e^{jwt} is omitted):

$$E_r \approx E_{theta} \approx H_r \approx H_{phi} \approx 0$$

$$H_{theta} \approx -E_{phi}/\eta \qquad (\eta \text{ is the intrinsic impedance of free space})$$

$$E_{phi} \approx -j\frac{V_o W k_o e^{-jkor}}{\pi r}\left[\frac{\sin[(k_o h/2)\sin\theta\cos\Phi]}{[(k_o h/2)\sin\theta\cos\Phi]}\right]\left[\frac{\sin[(k_o W/2)\cos\theta]}{[(k_o W/2)\cos\theta]}\right]$$

$$\bullet\sin\theta \bullet\cos[(k_o L/2)\sin\theta\sin\Phi] \quad (V/M);\ 0\leq\theta\leq\pi,\ (\pi/2)\leq\Phi\leq(3\pi/2) \qquad (3-3)$$

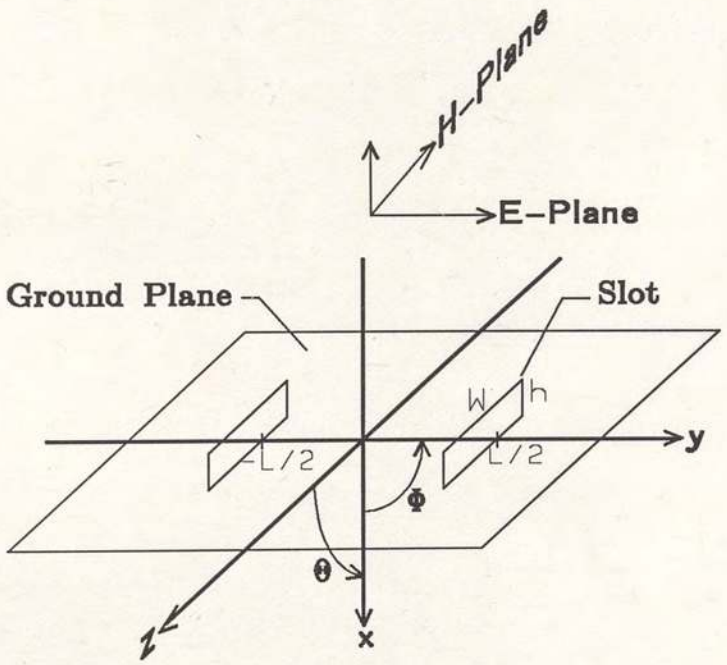

Figure 5. Coordinate System for Field Calculation.

*Far field is a distance from the antenna greater than $2D^2/\lambda_o$, where D is the maximum antenna dimension. In the far field, the radiation intensity pattern is independent of distance.

where $V_o = (h)(\mathbf{E}_{aperture})$ is the voltage across each slot, the propagation constant $k_o = 2\pi/\lambda_o = \omega\sqrt{\mu_o \epsilon_o}$, r is the distance from the origin to the far field observation point, and $\cos[(k_o L/2)\sin\theta\sin\Phi]$ is the array factor. The factor $|(k_o h/2)\sin\theta\cos\Phi|$ will vary from 0 to $(k_o h/2)$. Looking ahead at experimental data, $(k_o h/2)$ is about 0.3 (using $k_o = 2\pi/\lambda_o$, $h_{max} = \lambda_o/10$). Therefore, the first sin(X)/X form term in equation 3-1 above will vary from 1 to .98507 (0 to -.13dB). This can be approximated to 1 (odb). The normalized far field radiation intensity* pattern can be calculated from the **E** field as:

$$U_{normalized} = [(r^2/2\eta)|\mathbf{E}|^2]_{normalized}$$

$$\approx [(r^2/2\eta)|E_{phi}|^2]_{norm} \text{ (Watts/unit solid angle)} \qquad (3-4)$$

where | | indicates magnitude and η is the intrinsic impedance of free space ($120\pi\ \Omega$). The E & H-plane** radiation intensity patterns, using the coordinates of Figure 5, the approximation of 1 for the first sinX/X term, letting $(k_o L/2) = \pi/(2\sqrt{\epsilon_r})$ and L = W for the square patch, are:

---

*$U = r^2 W_{rad} = r^2\{(1/2)\mathrm{Re}[\mathbf{EXH}^*]\}$ where U is the far field radiation intensity at a point and W_{rad} is the average power density at a point. Since, in the far field, $|H| \approx |E/\eta|$, then equation 3-4 results.

**E and H-Planes are the planes containing the E or H field vector, respectively, and the direction of maximum radiation.

E–Plane ($\theta=\pi/2$):

$$U_{norm} \approx \cos^2[\pi/(2\epsilon_r^{1/2})\sin\Phi] \quad (W/SR); \quad \pi/2 \leq \Phi \leq 3\pi/2, \; h<<\lambda \qquad (3-5)$$

H–Plane ($\Phi=\pi$):

$$U_{norm} \approx \left[\frac{\sin[\pi/(2\epsilon_r^{1/2})\cos\theta]}{[\pi/(2\epsilon_r^{1/2})\cos\theta]} \right]^2 \bullet \sin^2\theta \quad (W/SR); \; 0 \leq \theta \leq \pi, \; h<<\lambda \qquad (3-6)$$

Changing variables to the coordinate system of Figure 4(a), the E and H–Plane power patterns are:

E–Plane ($\Phi=0$):

$$U_{norm} \approx \cos^2[\pi/(2\epsilon_r^{1/2})\sin\theta] \quad (W/SR); \; -\pi/2 \leq \theta \leq \pi/2, \; h<<\lambda \qquad (3-7)$$

H–Plane ($\Phi=\pi/2$):

$$U_{norm} \approx \left[\frac{\sin[\pi/(2\epsilon_r^{1/2})\sin\theta]}{[\pi/(2\epsilon_r^{1/2})\sin\theta]} \right]^2 \bullet \cos^2\theta \; (W/SR); \; -\pi/2 \leq \theta \leq \pi/2, h<<\lambda \qquad (3-8)$$

Bahl and Bhartia's calculations [1] position the edge radiator slot in the same plane as the patch in determining the E field. After the approximation done above, this yields the same radiation patterns as above. However, if dielectric thickness (h) is increased to the point where the slots are directional, Bahl's calculations will suffer in the H plane and they should be considered in error.

The two-layer patch antenna is expected to show similar pattern results to the single layer element discussed above. Coupling from the feed will excite a resonant mode for the element and the radiating edges of the upper patch will form slots with the ground plane. However, the **E** field will pass through two dielectrics (ϵ_{rU} and ϵ_{rL}, Figure 3) giving a different **E** in each dielectric. Assuming the region is charge free, the electric flux density **D** (**D**=ϵ**E**) will be constant. This yields $(\epsilon_{rU})(\mathbf{E}_U)=(\epsilon_{rL})(\mathbf{E}_L)$ or $\mathbf{E}_U=(\epsilon_{rL}/\epsilon_{rU})(\mathbf{E}_L)$ where $_U$ and $_L$ indicate the upper and lower dielectric regions, respectively. Therefore, for the two-layer design, a first-order approximation is that the radiation is a combination of two **E** fields which, being very close ($h<<\lambda$) essentially radiate from the same point. Using equation (3-3), the far zone electric field **E** for the two-layer design is:

$$E_{phi} \approx [E_{phi} \text{ of eq.(3-3) with } V_o=(h_U)(E_{U_{aperture}}) \text{ and } \epsilon_r = \epsilon_{rU}] + [E_{phi} \text{ of eq.(3-3) with } V_o=(h_L)(E_{L_{aperture}}) \text{ and } \epsilon_r = \epsilon_{rL}] \quad (3-9)$$

Using the approximation for small h, and the coordinates of Figure 5, the E and H plane radiation intensities for the two-layer design are:

E-Plane ($\theta=\pi/2$):

$$U_{norm} \approx \left[\frac{h_U(\epsilon_{rL}/\epsilon_{rU})\cos[\pi/(2\epsilon_{rU}^{1/2})\sin\Phi] + h_L \cos[\pi/(2\epsilon_{rL}^{1/2})\sin\Phi]}{h_U(\epsilon_{rL}/\epsilon_{rU}) + h_L} \right]^2$$

(W/SR); $\pi/2 \leq \Phi \leq 3\pi/2$, $h<<\lambda$ (3-10)

H–Plane ($\Phi=\pi$):

$$U_{norm} \approx \left[\frac{h_U(\epsilon_{rL}/\epsilon_{rU})\{\sin(X_1)/X_1\} + h_L\{\sin(X_2)/X_2\}}{h_U(\epsilon_{rL}/\epsilon_{rU}) + h_L}\right]^2 \cdot \sin^2\theta$$

$$(W/SR);\ 0 \leq \theta \leq \pi,\ h << \lambda, \qquad (3-11)$$

where $X_1=[\pi/(2\sqrt{\epsilon_{rU}})\cos\theta]$ and $X_2=[\pi/(2\sqrt{\epsilon_{rL}})\cos\theta]$. Changing variables to the coordinate system of Figure 4(a), the E and H–plane power patterns are:

E–Plane ($\Phi=0$):

$$U_{norm} \approx \left[\frac{h_U(\epsilon_{rL}/\epsilon_{rU})\cos[\pi/(2\epsilon_{rU}^{1/2})\sin\theta] + h_L\cos[\pi/(2\epsilon_{rL}^{1/2})\sin\theta]}{h_U(\epsilon_{rL}/\epsilon_{rU}) + h_L}\right]^2$$

$$(W/SR);\ -\pi/2 \leq \theta \leq \pi/2,\ h << \lambda \qquad (3-12)$$

H–Plane ($\Phi=\pi/2$):

$$U_{norm} \approx \left[\frac{h_U(\epsilon_{rL}/\epsilon_{rU})\{\sin(X_1)/X_1\} + h_L\{\sin(X_2)/X_2\}}{h_U(\epsilon_{rL}/\epsilon_{rU}) + h_L}\right]^2 \cdot \cos^2\theta$$

$$(W/SR);\ -\pi/2 \leq \theta \leq \pi/2,\ h << \lambda \qquad (3-13)$$

where $X_1=[\pi/(2\epsilon_{rU}^{1/2})\sin\theta]$ and $X_2=[\pi/(2\epsilon_{rL}^{1/2})\sin\theta]$. As mentioned earlier, the lower substrate of the proposed two–layer design has a high permittivity and the upper substrate is a low permittivity. This means that $\epsilon_{rL}/\epsilon_{rU} > 1$ ($\approx$2.7 to 4.77). Also, for proper matching it turns out that $h_U > h_L$. Therefore, using these concepts in the theoretical equations above, the high dielectric of the lower layer, useful for integration of feed structures

but usually troublesome to patch radiation, has little effect on the two-layer design radiation pattern.

Linear plots of the E and H plane radiation intensity patterns for thin single layer patch elements using equations 3-7 and 3-8 are shown for various dielectrics in Figure 6. Similar plots for the two-layer design using equations 3-12 and 3-13 for various thicknesses and dielectrics are shown in Figure 7. The plots were generated with a FORTRAN program on an Apollo computer.

Directivity* (D_o) is calculated as $4\pi U_{max}/P_{rad}$ where P_{rad} is the total power radiated from the antenna. Using the coordinates of Figure 5, the microstrip patch half-space radiator has directivity:

$$D_o = \frac{4\pi\, U_{max(norm)}(\theta=\pi/2,\Phi=\pi)}{\int_{\Phi=\pi/2}^{3\pi/2}\int_{\theta=0}^{\pi} U_{norm}\sin\theta\, d\theta\, d\Phi} \quad \text{(Dimensionless)} \quad (3\text{-}14)$$

where U_{norm} is obtained from equations 3-4 and 3-3. A FORTRAN program was used to numerically perform the power radiated integral and calculate the directivity. Table 2 shows the directivities for the

*Directivity is the maximum radiation intensity relative to an isotropic source or $D_o = U_{maximum}/U_{isotropic}$. $U_{isotropic} = P_{rad}/4\pi$ since there are 4π steradians in a sphere.

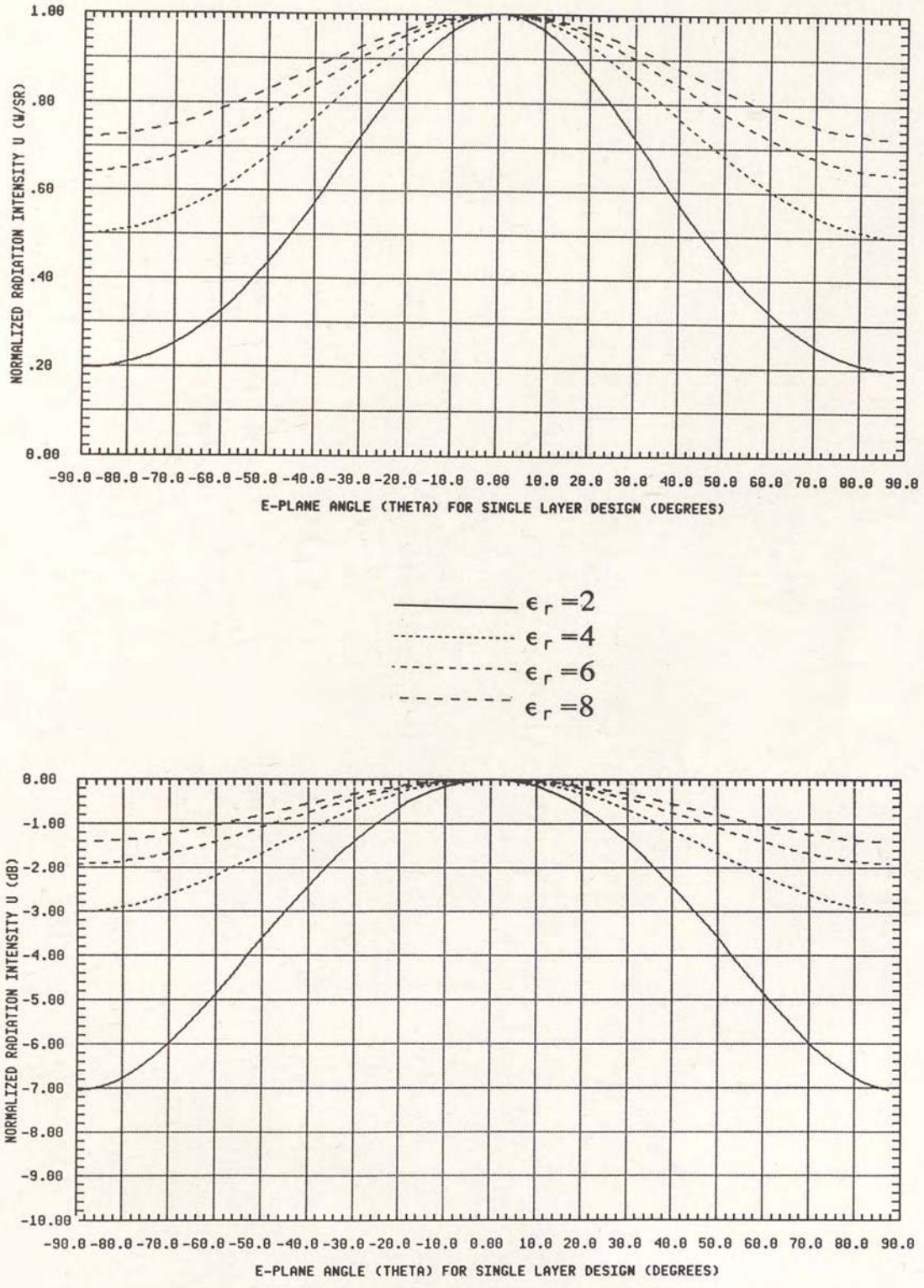

Figure 6(a). Theoretical Single Layer Patch E–Plane Radiation Intensity Pattern using Figure 4(a) Coordinates.

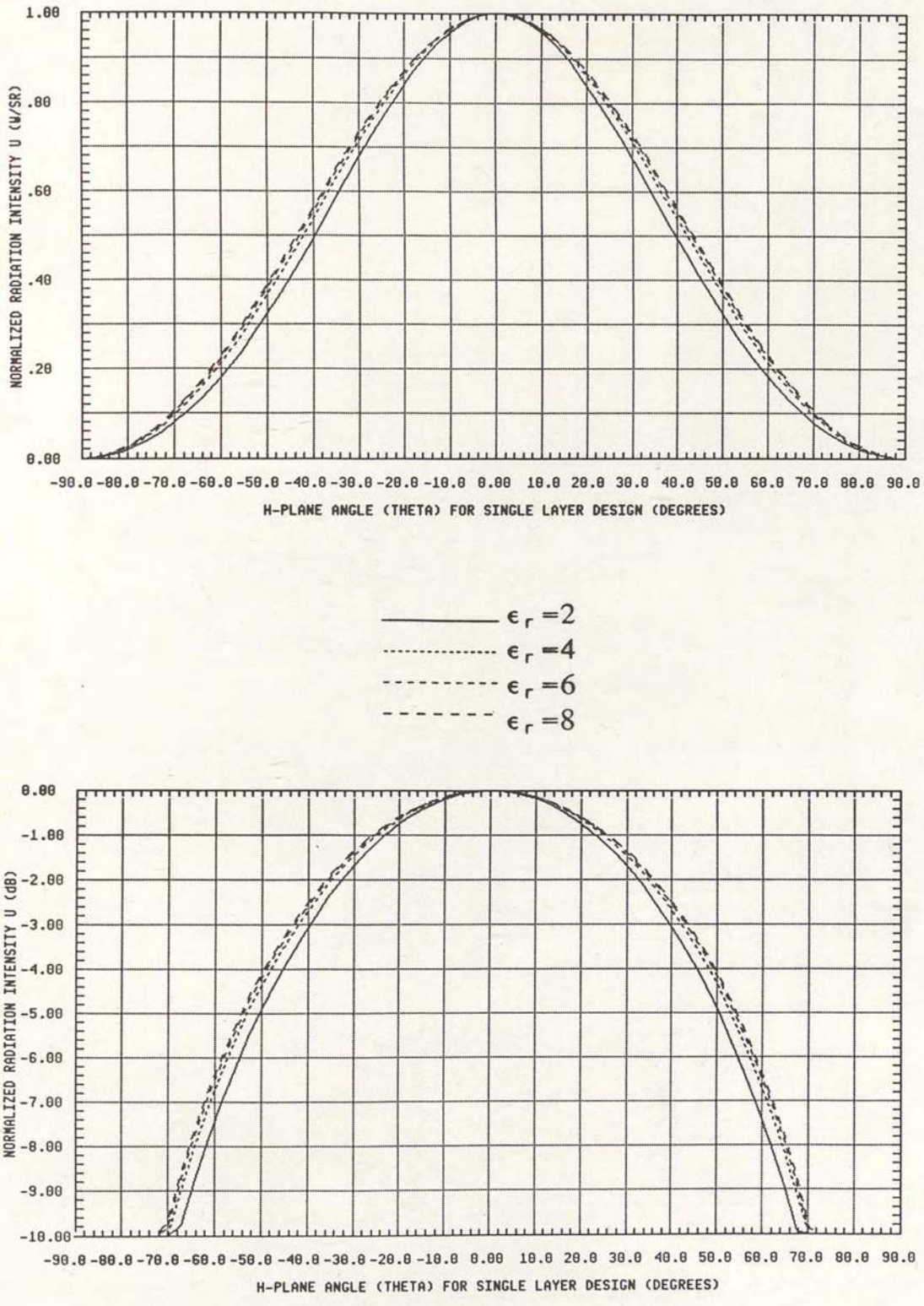

Figure 6(b). Theoretical Single Layer Patch H–Plane Radiation Intensity Pattern using Figure 4(a) Coordinates.

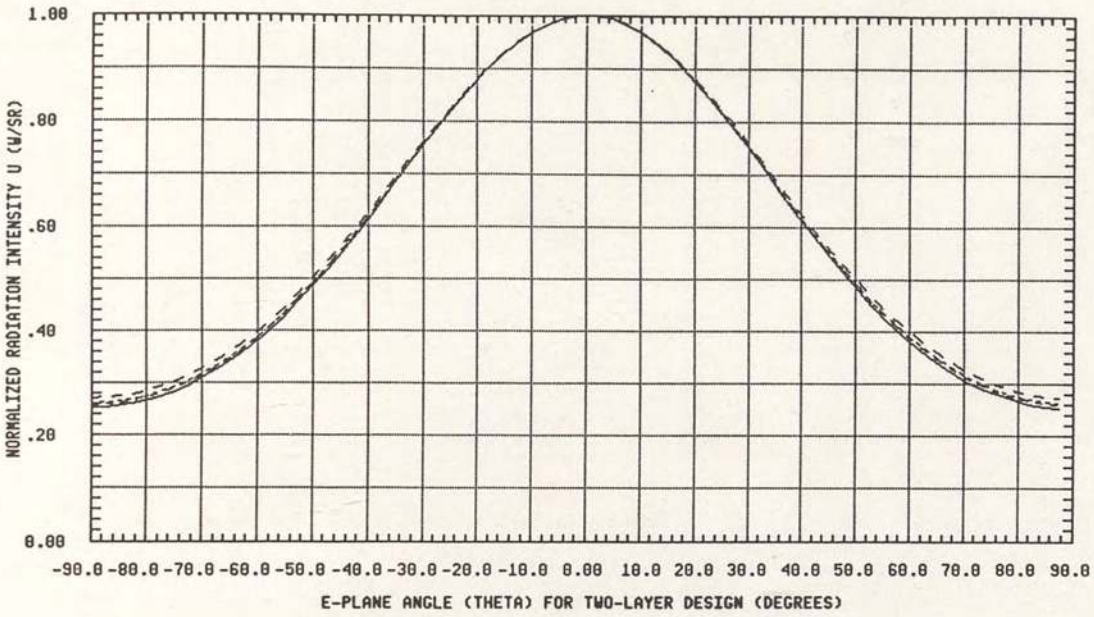

———— ϵ_{rL}=10.5, h_L=.010″, ϵ_{rU}=2.2, h_U=.062″
····· ϵ_{rL}=10.5, h_L=.025″, ϵ_{rU}=2.2, h_U=.092″
- - - - - ϵ_{rL}=10.5, h_L=.025″, ϵ_{rU}=2.2, h_U=.102″
— · — · — ϵ_{rL}= 6.0, h_L=.025″, ϵ_{rU}=2.2, h_U=.082″

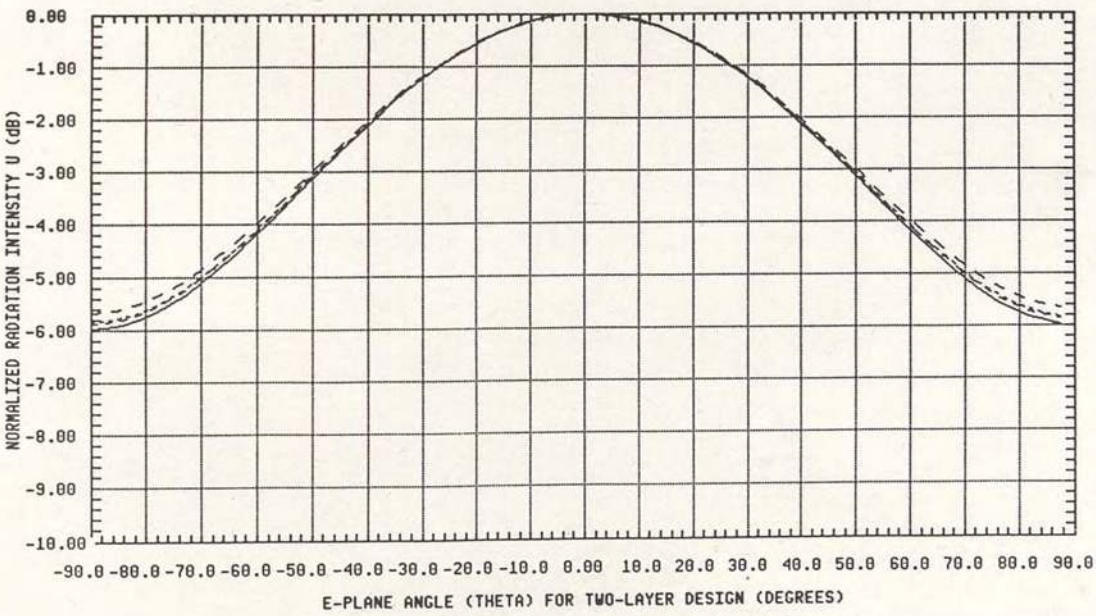

Figure 7(a). Theoretical Two-Layer Patch E-Plane Radiation Intensity Pattern using Figure 4(a) Coordinates.

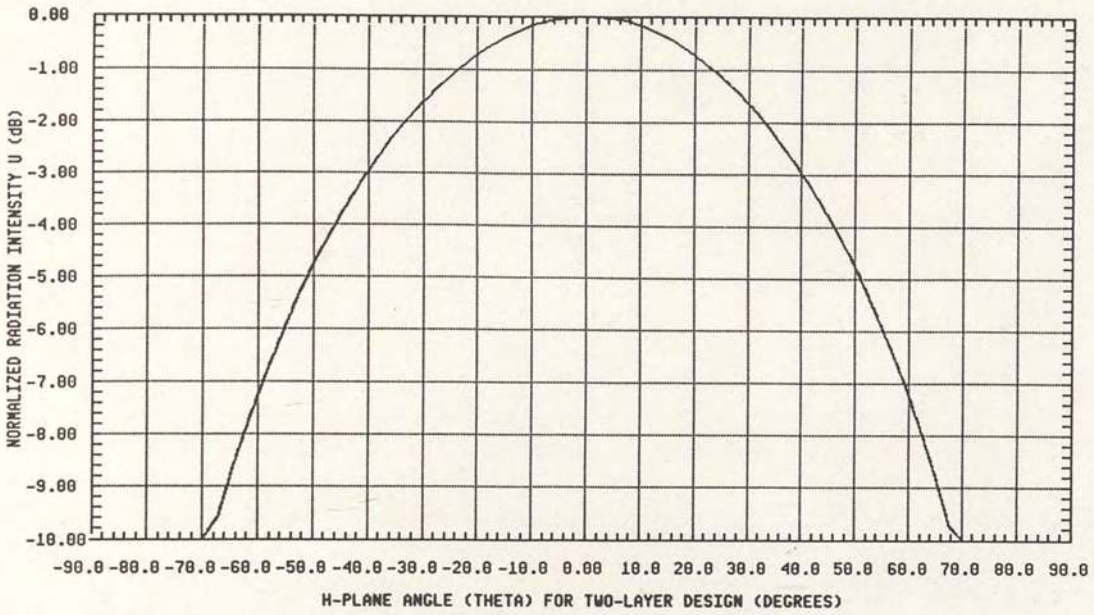

———— ϵ_{rL}=10.5, h_L=.010″, ϵ_{rU}=2.2, h_U=.062″
····· ϵ_{rL}=10.5, h_L=.025″, ϵ_{rU}=2.2, h_U=.092″
- - - - - ϵ_{rL}=10.5, h_L=.025″, ϵ_{rU}=2.2, h_U=.102″
— — — — ϵ_{rL}= 6.0, h_L=.025″, ϵ_{rU}=2.2, h_U=.082″

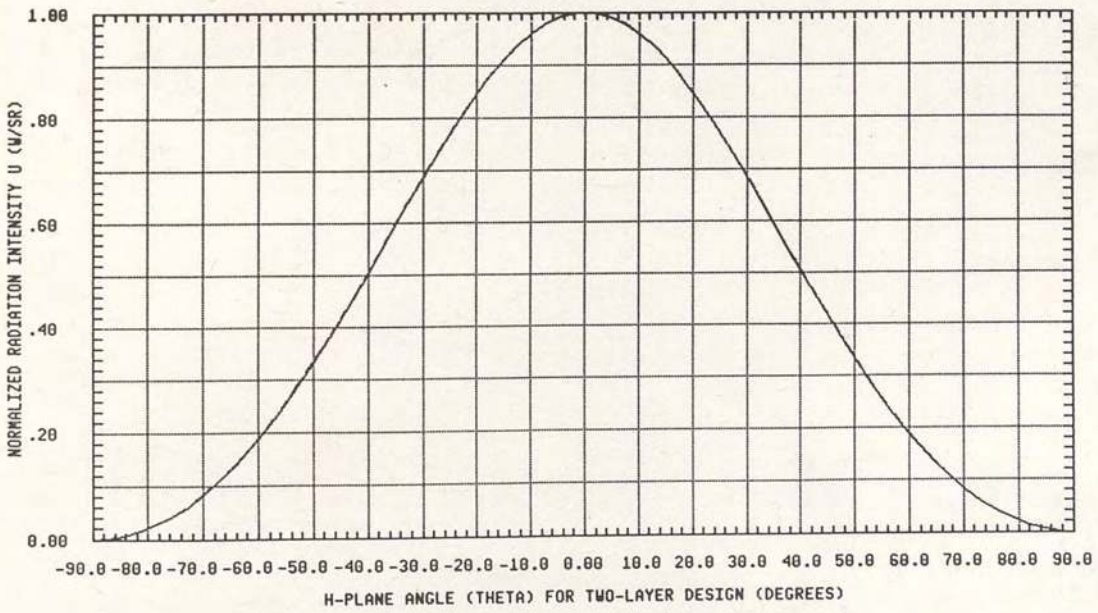

Figure 7(b). Theoretical Two–Layer Patch H–Plane Radiation Intensity Pattern using Figure 4(a) Coordinates.

configurations whose principal plane patterns were plotted in figures 6 and 7. The patterns, and therefore the directivity, of the two-layer configurations plotted in Figure 7 are nearly identical to a single layer element with $\epsilon_r = 2.2$.

TABLE 2.

THEORETICAL DIRECTIVITY OF MICROSTRIP PATCH ANTENNA ELEMENTS

PARAMETERS	DIRECTIVITY D_o (dimensionless)	DIRECTIVITY D_o (dBi)=10logD_o	GAIN(dBi) $G_o = e_t D_o$ @$e_t = .8$
$\epsilon_r = 2$ single layer	5.284	7.23	6.26
$\epsilon_r = 4$ single layer	3.997	6.02	5.05
$\epsilon_r = 6$ single layer	3.634	5.60	4.63
$\epsilon_r = 8$ single layer	3.464	5.40	4.43
$\epsilon_{rU} = 2.2, h_U = .062$ two-layer $\epsilon_{rL} = 10.5, h_L = .010$	4.959	6.95	5.98
$\epsilon_{rU} = 2.2, h_U = .092$ two-layer $\epsilon_{rL} = 10.5, h_L = .025$	4.915	6.92	5.95
$\epsilon_{rU} = 2.2, h_U = .102$ two-layer $\epsilon_{rL} = 10.5, h_L = .025$	4.926	6.93	5.96
$\epsilon_{rU} = 2.2, h_U = .082$ two-layer $\epsilon_{rL} = 6.0, h_L = .025$	4.863	6.87	5.90

The gain ($G_o = e_t D_o$) of the antenna takes into account the total efficiency e_t as well as the directivity. For the microstrip patch antenna, lower than 100% efficiency is the result of losses including mismatch, conduction losses, dielectric losses, and power lost to a surface wave along the dielectric [3, 5]. A well matched, thin microstrip antenna element is assumed, so that mismatch and surface wave losses are negligible. Conduction power losses (I^2R type) are due to the non-zero resistivity ($R_s \neq 0$) of the patch and ground plane. They can be calculated from the currents induced in the patch and ground plane by the tangential magnetic fields (H_t) inside the patch cavity. The dielectric losses (V^2/R type) are a result of the non-zero conductivity of the dielectric ($\sigma_d \neq 0$) and can be calculated from the electric (E) field inside the dielectric filled patch cavity. Using the coordinates of Figure 4(a), the power loss for the microstrip patch antenna takes the form [2, 3, 9]:

$$P_{loss} = (R_s/2)\left[2\int_0^W\int_0^L |H_t|^2\,dxdy\right] + h\sigma_d \int_0^W\int_0^L |E_z|^2\,dxdy \quad \text{Watts} \qquad (3\text{-}15)$$

where the resistivity of the conductor $R_s = (\omega\mu/2\sigma_c)^{-1/2}$ Ω/square, σ_c is the conductivity of the conductor, $\sigma_d = \omega_r \epsilon_r \epsilon_o \tan\delta$ (S/M), $\tan\delta$ is the loss tangent of the dielectric, and $\omega_r = 2\pi f_r$ where r indicates resonance. For copper conductors ($\sigma_c = 5.80 \times 10^7$ S/M) etched on a 0.062" thick dielectric of RT Duroid 5880 ($\tan\delta = .0009$, $\epsilon_r = 2.2$ at 10GHz) at an X band resonant

frequency (10GHz), then R_s=0.0261 Ω/square, and $h\sigma_d$=0.0011 S. This indicates that equation 3–15 will be a low percentage of the input power, yielding a high overall efficiency e_t ($e_t = P_{rad}/[P_{rad}+P_{loss}]$). The complex architecture of the two–layer microstrip patch element creates a non–trivial solution for the **E** and **H** fields inside the dielectric cavity structures. It is assumed that power losses will be on the order of a single layer design of comparable thickness. Table 2 lists the gains of several elements using a reasonable to low efficiency of 80%.

Resonant Frequency

For the standard single layer patch element, the region between the microstrip patch and the ground plane can be treated as a thin, dielectric loaded, transverse magnetic (TM) mode cavity [2, 3, 4, 5]. The cavity is bounded by electric walls above and below and by magnetic walls (open circuit) on the sides. Figure 4(c) shows a cross section and E field distribution inside the TM_z mode cavity. The field components, solved subject to the boundary conditions of zero tangential magnetic field at the four sides of the cavity, are exactly the duals of the well known rectangular waveguide transverse electric (TE) modes. The resonant frequency (f_r) of the patch cavity is calculated as the cut off frequency in this guide:

$$f_{r\,mn} = \{1/[2\pi(\mu_o \epsilon_o \epsilon_r)^{1/2}]\}\ \{(m\pi/L)^2 + (n\pi/W)^2\}^{1/2} \qquad (3\text{–}16)$$

where $_{mn}$ represents the mode of the cavity. The described cavity model is not exact, since a true closed cavity would have no fringing fields and no radiated power. The theory has been modified to account for the fringing and radiation by introducing a factor to slightly increase the cavity length (L) and using a complex wall admittance at the open circuits. This model has given good results in the references listed above. From equation 3-16, the fundamental half wave resonance mode is the m=1, n=0 mode (1,0 or TM_{10} mode). For the square patch (L=W), the (0,1) mode is degenerate (resonant at the same frequency). When narrowbanding around this fundamental resonance, Carver and Mink [3] have shown that the higher order modes have negligible loss and sum to form a small series inductance to the input impedance. Concentrating on the fundamental resonance (TM_{10}) mode, inserting m=1 and n=0 into equation 3-16, the resonant frequency is:

$$f_r = \frac{c}{2L(\epsilon_r)^{1/2}} \qquad (3-17)$$

where the speed of light $c=1/(\mu_o \epsilon_o)^{1/2}=2.998x10^{10}$ cm/sec. This calculation for f_r needs to be modified to account for fringing fields. Since these fields extend slightly at the patch ends into the air above the substrate (see Figure 4c), passing through two dielectric regions, a combination or effective dielectric constant results. This is similar to the effective dielectric used for microstrip lines. Schneider [10] empirically solved for this effective dielectric (ϵ_e):

$$\epsilon_e = \frac{\epsilon_r+1}{2} + \left[\frac{\epsilon_r-1}{2}\right]\left[\frac{1}{(1+10h/W)^{1/2}}\right] \qquad (3-18)$$

Also, the fringing fields tend to increase the size of the cavity in the L direction by ΔL on each radiating end of the patch. An empirical formula for ΔL reported in [3] and [1] is the result of E.O. Hammerstad's work:

$$\Delta L = 0.412h\left[\frac{\epsilon_e+0.300}{\epsilon_e-0.258}\right]\left[\frac{(W/h)+0.264}{(W/h)+0.800}\right] \qquad (3-19)$$

Replacing L by (L+2ΔL) and ϵ_r by ϵ_e in equation 3-17, the resonant frequency of the single layer rectangular patch antenna is predicted as [1,11]:

$$f_r = \frac{c}{2(L+2\Delta L)(\epsilon_e)^{1/2}} \qquad (3-20).$$

The effective dielectric for an air covered microstrip line (equation 3-18) is less than ϵ_r of the substrate. This lowered dielectric constant results in a higher resonant frequency. However, this increase is offset by the increase in microstrip patch length of 2ΔL.

The resonant frequency of the two-layer microstrip patch design (Figure 3) will be perturbed by both the presence of the two dielectrics, and the coupling between the two patches. Resonance occurs when the energy stored in the E and H fields is equal, being transferred back and forth over time. Since the fields will be affected by the coupling and dielectrics, the resonant

frequency will shift to accommodate this change. However, the major factors affecting resonant frequency should be the patch dimension L and the dielectric constant ϵ_e. A first-order approach proposed here to determine the resonant frequencies of the two-layer design is to divide the configuration into two special cases of a single layer patch element and determine the resonance of each. The two resonances together should form the return loss response of Figure 2. The dielectric effects are accounted for in this approach but the coupling effects on resonant frequency are neglected. Figure 8 shows the division, for calculation purposes, of the

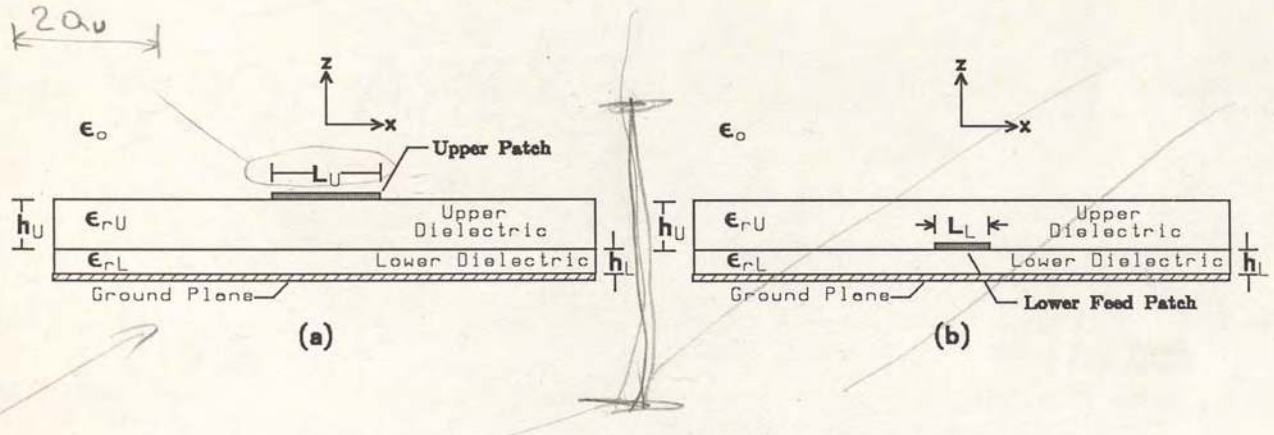

Figure 8. Division of the Two-Layer Microstrip Patch Element for Resonant Frequency Calculation.

two-layer microstrip patch element design into a single patch etched on a double dielectric (a), and a single patch element with a dielectric cover (b). It is reasonable to assume that the resonant frequency of the upper patch of Figure 8(a) can be calculated from equations 3-18, 3-19, and 3-20 by replacing ϵ_r with a resultant dielectric constant ϵ_{rc} due to the combination

of ϵ_{rL} and ϵ_{rU}. A method which seems feasible to derive ϵ_{rc} is to use the static condition of constant electric flux density D_z ($\mathbf{D}=\epsilon\mathbf{E}$) through the two dielectrics, from an applied voltage $V_o = hE_z$:

$$V_o = h_L(D/\epsilon_o\epsilon_{rL}) + h_U(D/\epsilon_o\epsilon_{rU}) = (h_L+h_U)(D/\epsilon_o\epsilon_{rc}) \qquad (3-21)$$

which yields:

$$\epsilon_{rc} = (h_L+h_U)(\epsilon_{rL}\epsilon_{rU}) \,/\, (h_L\epsilon_{rU} + h_U\epsilon_{rL}) \qquad (3-22)$$

Therefore, the theoretical resonant frequency is calculated from equations 3–18, 3–19, 3–22, and 3–20 by using $\epsilon_r=\epsilon_{rc}$, $h=h_L+h_U$, W=L in 3–18 and $h=h_L+h_U$, W = L in 3–19. Figures 9 and 10 graphically display results of equations 3–17 through 3–22 for resonant frequencies in X band. Figure 9 shows the relationship between resonant frequency before and after adding the lower dielectric. It is clear that the addition of the high dielectric layer increases the effective dielectric constant and thus decreases the resonant frequency. Figure 10 depicts the resonant frequency versus patch length L for upper dielectric thicknesses set to .042″, .062″, .082″, and .102″, an upper dielectric constant of 2.2 and various lower dielectric constants and thicknesses. The plots were done in FORTRAN on an Apollo computer. Parameters chosen to be plotted (dielectric constants and thicknesses) are based on readily available substrate material and preliminary experimental data.

Using the configuration of Figure 8(b), limits on the lower feed patch resonance can be determined from the two extremes of an air covered patch (no upper dielectric) and an infinite dielectric cover of the same high dielectric constant. The resonance of the air covered case is calculated from equations 3–18, 3–19 and 3–20 as for a standard single layer microstrip patch element. The air cover will produce the lowest effective dielectric of any practicable cover and therefore the highest resonant frequency. This is the upper limit of the expected resonance of the lower feed patch. An infinite upper dielectric cover with dielectric constant ϵ_{rL} will form the lower limit of the expected resonance. Logically, if the cover approaches infinity, and if the cover and patch substrate are of the same dielectric constant, then ϵ_e approaches ϵ_{rL}. This is confirmed in the work of [11]. Since this produces the highest effective dielectric, it yields the lowest resonant frequency. The effective dielectric of the two–layer patch element design will be somewhere in between the two extremes described since ϵ_{rU} is less than ϵ_{rL} but is greater than ϵ_r=1 of air. Figure 11 shows the results of calculations of the two extremes for several dielectric constants and thicknesses. The lower resonance is calculated from equations 3–19 and 3–20 with ϵ_e replaced by ϵ_{rL}. The gap between the extremes is seen to be less than 10% of the center frequency.

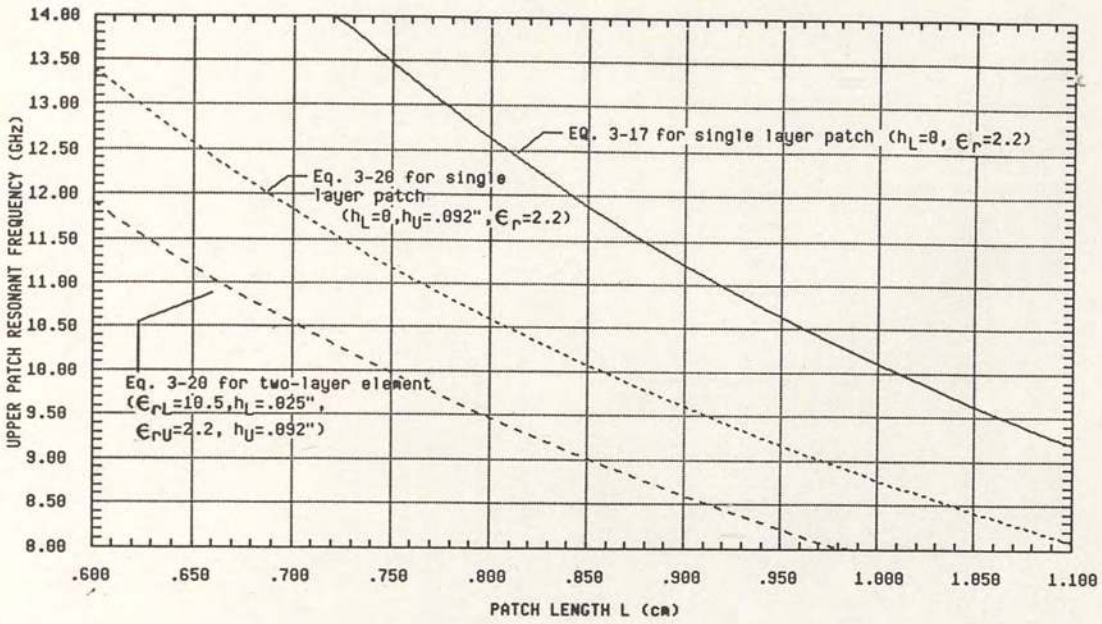

Figure 9. Relative Effects on Resonant Frequency of Single Versus Two-Layer Configuration.

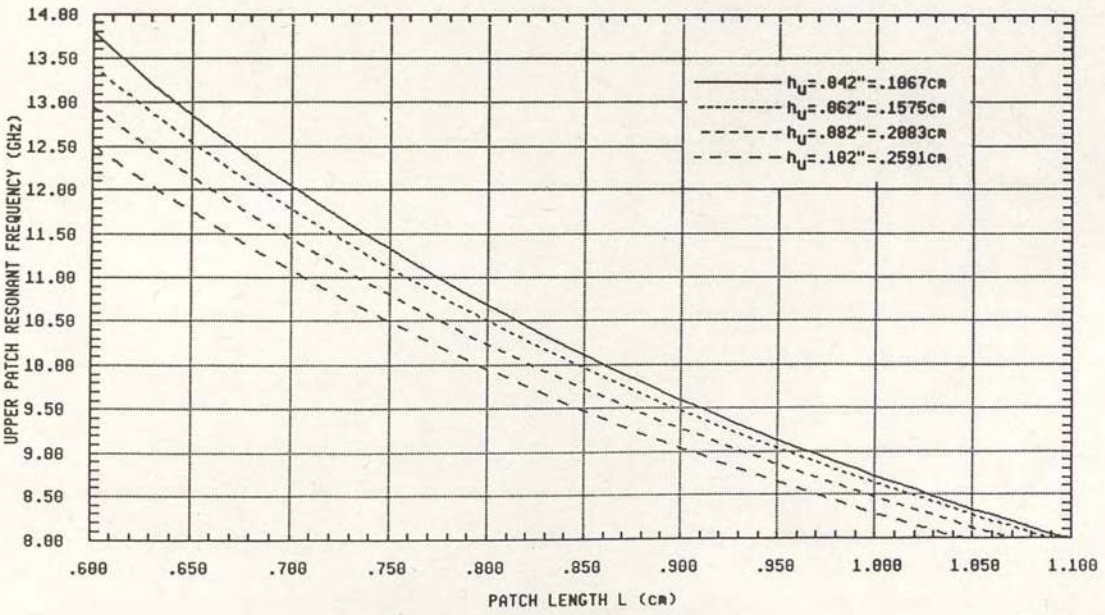

Figure 10(a). Theoretical Upper Patch Resonant Frequency Versus Patch Length for Several Upper Dielectric Thicknesses with $\epsilon_{rL}=10.5$, $h_L=.010"=.0254$cm, and $\epsilon_{rU}=2.2$.

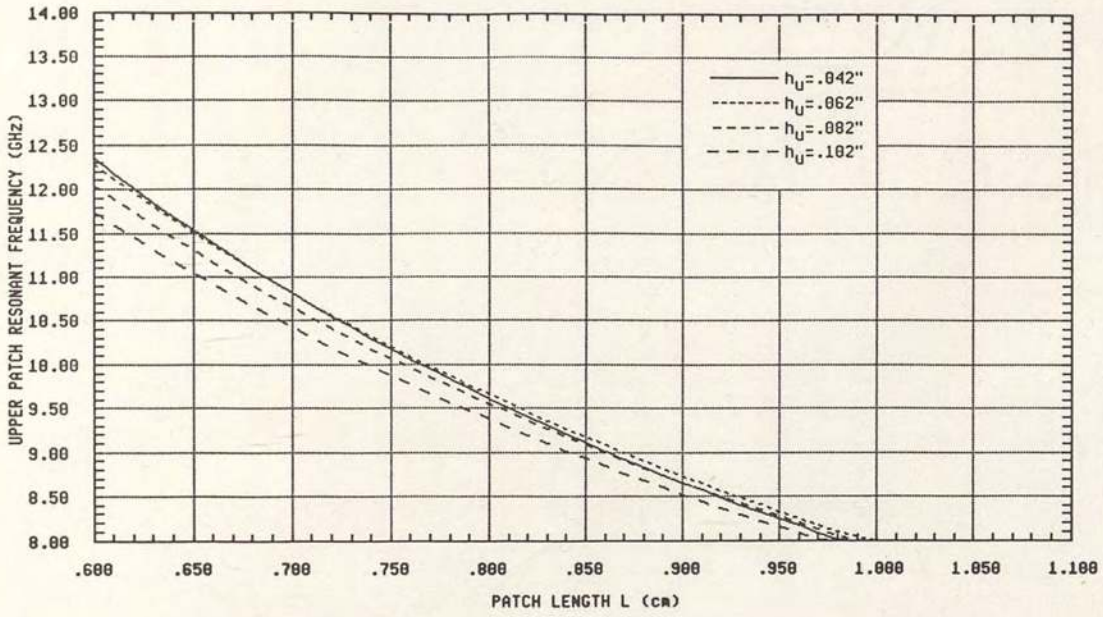

Figure 10(b). Theoretical Upper Patch Resonant Frequency Versus Patch Length for Several Upper Dielectric Thicknesses with $\epsilon_{rL}=10.5$, $h_L=.025''=.0635$cm, and $\epsilon_{rU}=2.2$.

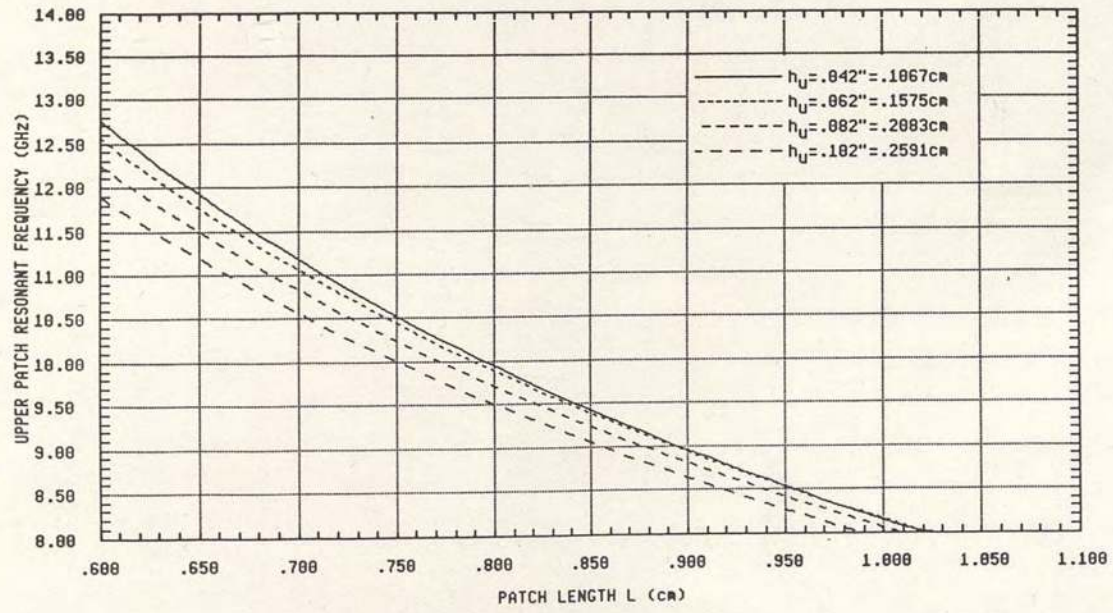

Figure 10(c). Theoretical Upper Patch Resonant Frequency Versus Patch Length for Several Upper Dielectric Thicknesses with $\epsilon_{rL}=6.0$, $h_L=.025''=.0635$cm, and $\epsilon_{rU}=2.2$.

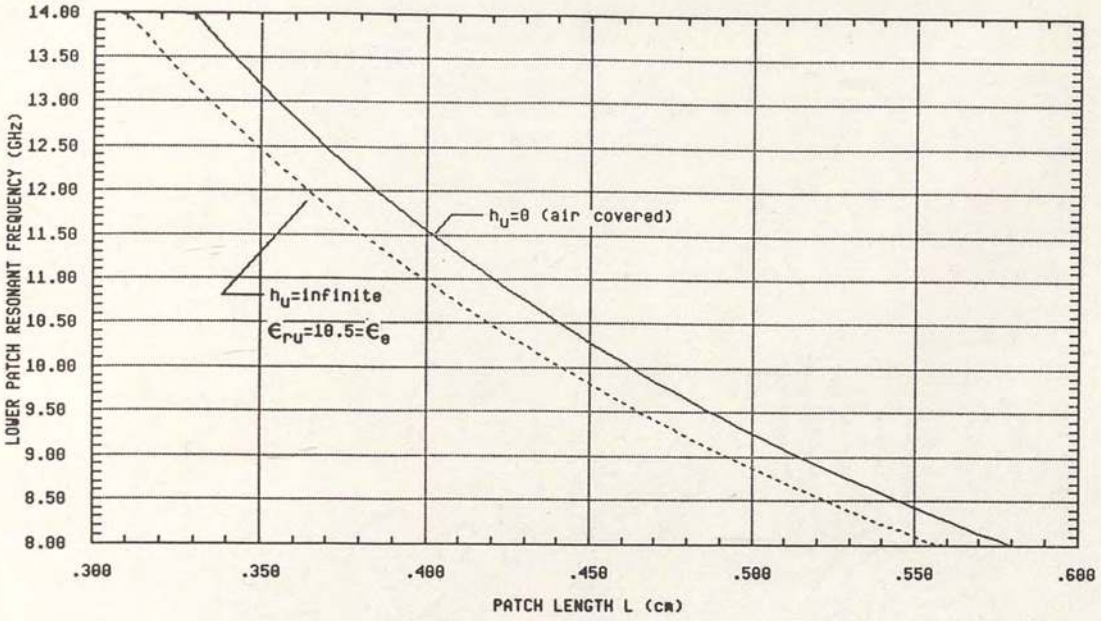

Figure 11(a). Theoretical Lower Patch Resonant Frequency Limits Versus Patch Length with $\epsilon_{rL}=10.5$, $h_L=.010''=.0254$cm

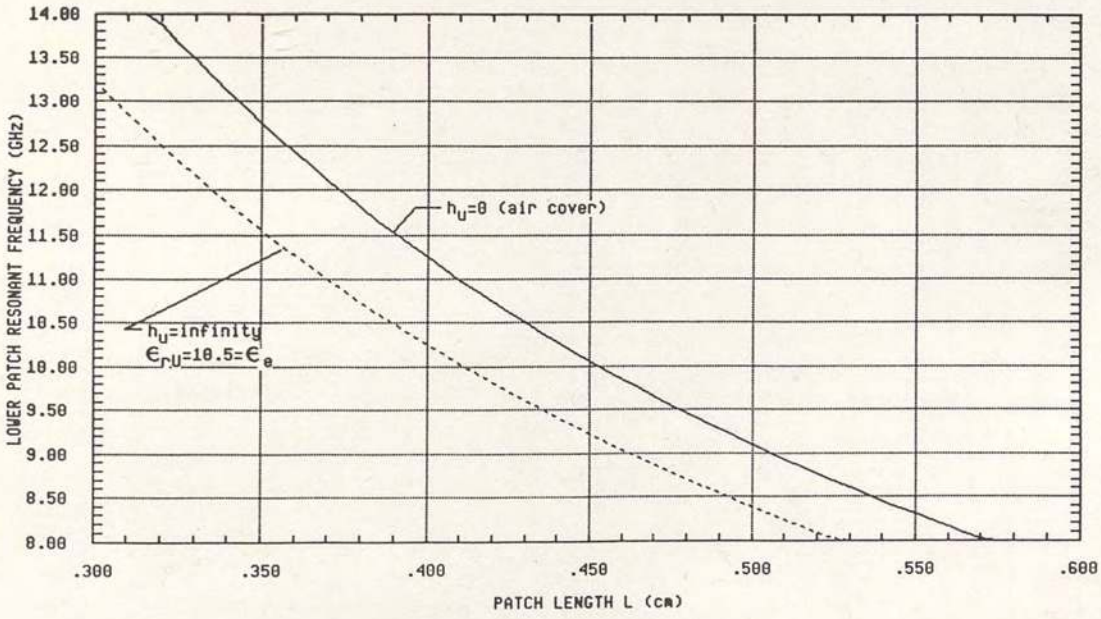

Figure 11(b). Theoretical Lower Patch Resonant Frequency Limits Versus Patch Length with $\epsilon_{rL}=10.5$, $h_L=.025''=.0635$cm

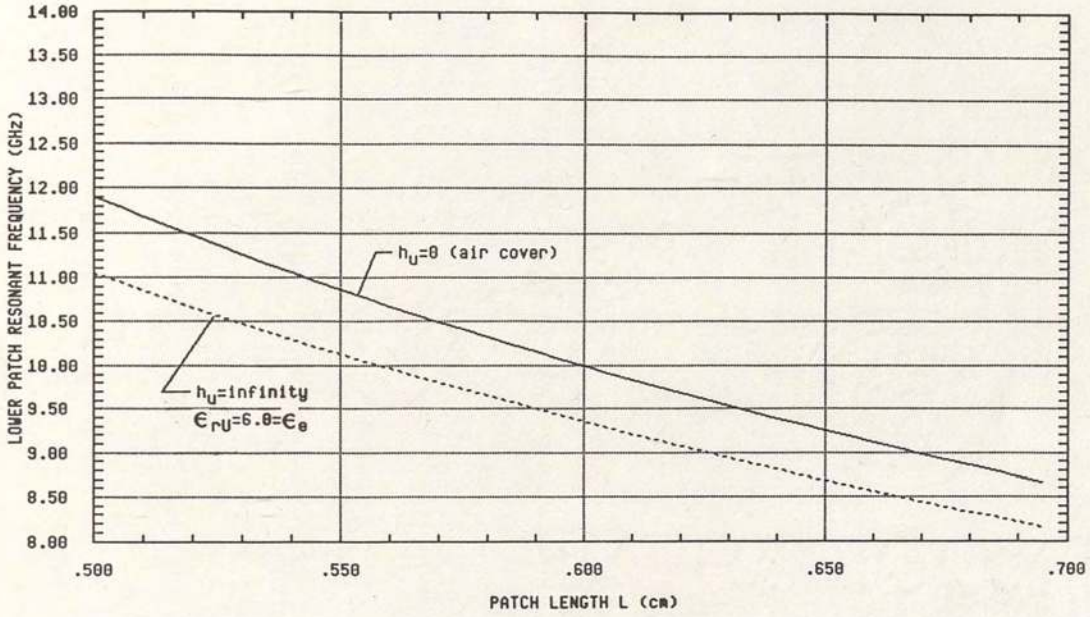

Figure 11(c). Theoretical Lower Patch Resonant Frequency Limits Versus Patch Length with $\epsilon_{rL}=6.0$, $h_L=.025''=.0635$cm

Input Impedance

A straightforward method for determining input impedance of microstrip patch antennas is with the transmission line model [3,6,7]. For the single layer patch, the element is modelled as a transmission line the same length as the patch and with characteristic impedance Z_o equal to that of a microstrip line of the same width and same dielectric. The line is terminated on each end with the admittance of the edge radiating slots. The input point to the line is at the same place as the feed point of the microstrip patch. The input impedance is found by transforming the end admittances to the feed point using standard transmission line equations. Resonance occurs at the frequency where the transformed slot susceptances cancel, theoretically yielding a real input impedance. In reality, coax connection through the substrate and higher order non-resonant modes add inductive reactance in series with the input [3].

For the two-layer microstrip element, the feed is not directly tied to the upper patch. However, following the direction of Oltman and Huebner's work [12], it is feasible that the coupling of the lower patch radiating edges to the upper patch can be modelled as transforming lines of some characteristic impedance connected to a typical transmission line model of the upper patch radiator. Oltman took this approach in modelling a patch parasitically coupled to an open circuit microstrip feed line. In his application there is only one radiating edge coupling to the patch. Oltman found that a wide range of input impedances occurred from the adjustment of

the dielectric height between the patch and the feed line, resulting from the change in coupling. In the model this is analogous to changing the tranforming line length and or characteristic impedance.

A transmission line model for the two-layer microstrip patch antenna will not be attempted here, but some important points result from its concept. The dual coupled transmission line model, resembling a double stub tuner, indicates that for the two-layer patch element, virtually any input impedance at a single frequency (including the best match condition for maximum power transfer) is possible by adjusting the dielectric heights. However, the condition of matching across a wide band of frequencies (more accurately matching at two closely spaced resonances) is seen to be a very special case of design parameters.

SECTION IV

EXPERIMENTAL PROCEDURE AND RESULTS

Several two-layer microstrip patch antenna elements were fabricated for linearly polarized, X band testing following the design outline described in Section II. The elements were fabricated in two parts, upper and lower patches, each using standard printed circuit technology. The upper patches were etched on RT Duroid* 5880 (ϵ_r=2.2, tanδ=.0009 at 10 GHz). The copper laminate on the underside was etched away so that no conducting layer was below this patch. Lower (feed) patches were etched on Duroid 6006 (ϵ_r=6.0, tanδ=.0027 at 10 GHz) and Duroid 6010.5 (ϵ_r=10.5, tanδ=.0028 at 10 GHz). The underside copper conducting layer of the feed patch is not etched and forms the ground plane of the assembled two-layer patch antenna element. The patch dimensions to be etched were chosen, using equation 3-20 (figures 10 and 11), for excitation of resonances throughout X band. Dielectric thicknesses of the fabricated elements are

---

*Duroid is the name Rogers Corporation gives to this non-woven glass reinforced, PTFE microwave substrate. The substrate is laminated with a copper foil and comes in a variety of thicknesses and dielectric constants. Rogers Corporation's product descriptions for Duroid 5880, 6006, and 6010.5 are given in Appendix B. An outline of materials and material problems (temperature effects and batch to batch dielectric change) can be found in [3].

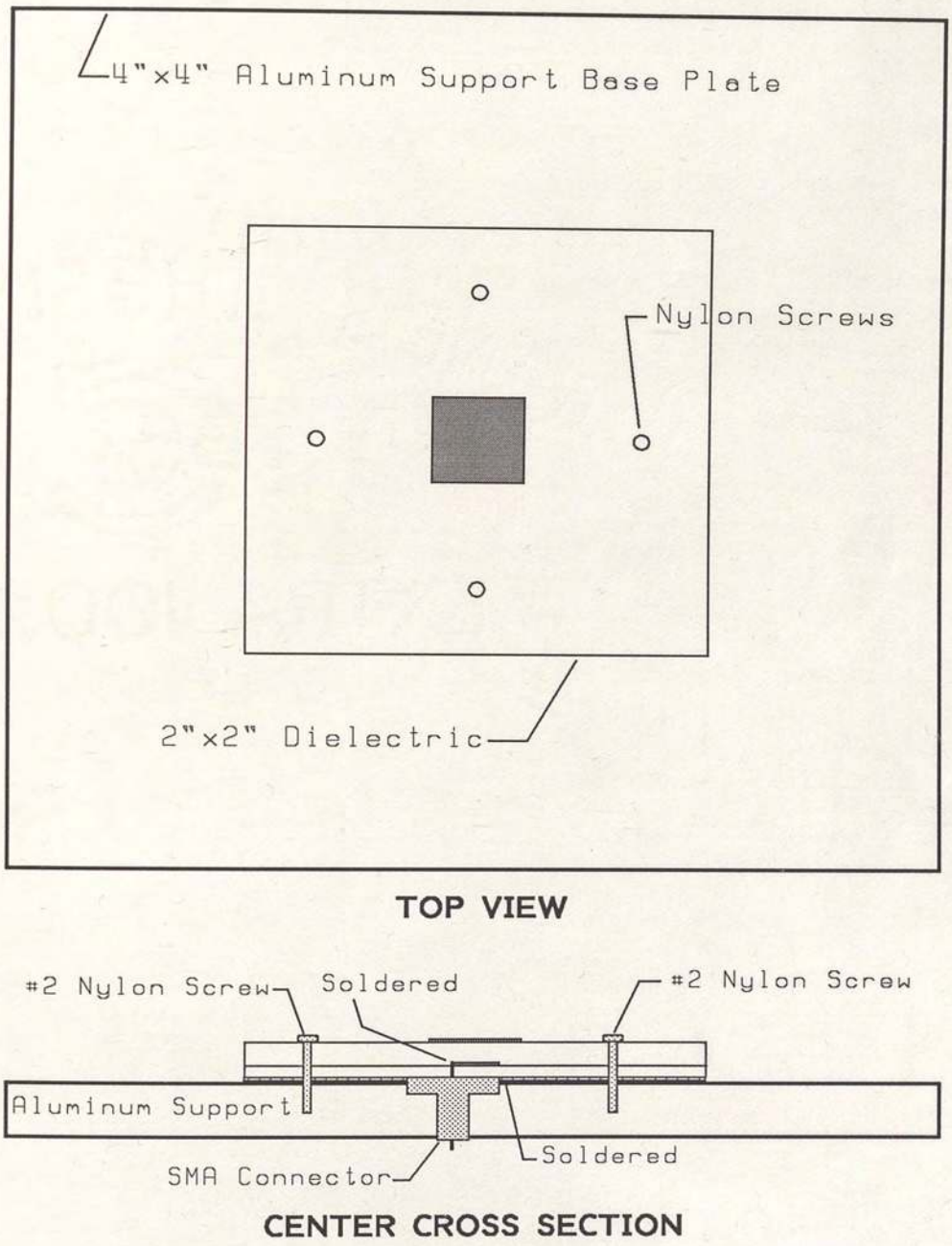

Figure 12. Two–Layer Microstrip Patch Antenna Element for Experiment.

those readily available from the manufacturer. In addition, several Duroid 5880 dielectric spacers were fabricated (copper laminate etched away from both sides leaving a bare dielectric sheet) for further adjustment of the upper patch dielectric thickness. A list of the elements fabricated and their dimensions is given in Appendix C.

The upper and lower patch parts are assembled into a two-layer patch antenna element as shown in Figure 12. The patches are stacked and bolted to an aluminum supporting base plate with nylon screws. Nylon was used to minimize extraneous effects on the fields of the antenna. Drill point rings (for marking the through holes to be drilled for the nylon screws) were etched on the dielectric with the same mask as the patch to assure accuracy of symmetrical allignment. Electrical connection is made to the lower feed patch with an SMA connector (VSWR<1.07 and insertion loss < .095dB at 10 GHz by Omni Spectra specifications). The center pin of each connector was cut and filled to extend through its particular lower element dielectric to a point a few mils below the top, and in the center of one edge, of the copper feed patch. The ground and pin of the connector were then soldered to the ground plane and feed patch, respectively. The solder at the pin connection was sanded flush with the top of the patch. This position of the SMA connector allows access directly to the feed edge of the patch, eliminating possible corruption of data from an interconnecting microstrip line. A hole in the aluminum base plate gives access to the connector when the two-layer element is assembled. Except for some minor problems listed

below, there was nothing to indicate that this fixture and assembly technique were other than very reliable. Repeatability of return loss response after reassembly was found to be within about 0 to 3 percent for resonant frequencies. The problems noted for the assembly of Figure 12 are:

- The fields in the lower patch cavity must be somewhat perturbed by the feed pin connection and the small etched circle in the ground plane (the etched circle is to accommodate the SMA connector dielectric). Good experimental results depict this not to be a major problem but its full extent is not known. An estimation of the extent of the problem can probably be found by attempting a repeat of the data using a microstrip feed line to the patch.

- Return loss response of assemblies with the thin .010″ feed could be shifted by putting pressure on the fixture edge (approximately 5% shift in resonant frequency). Since the fixture, when under test, was supported by the SMA connection, then probably the thin feed was warped by the pressure, allowing an air gap between the upper and lower patches. Care had to be taken in testing.

- Over time and use, the thin solder connection to the feed patch becomes fatigued and breaks.

Figures 13, 14 and 15 are in-depth experimental results of three different two-layer microstrip patch antenna elements, each of which displayed excellent broadband responses and, overall, performed as desired. Figure 16 depicts the results of a single layer patch design to be used for comparison. The two-layer configurations chosen for the figures were some of the better for the three feed element types of $\epsilon_{rL}=10.5$, $h_L=.025$; $\epsilon_{rL}=6.0$, $h_L=.025$; and $\epsilon_{rL}=10.5$, $h_L=.010''$. Working broadband two-layer configurations were found for these feed types by choosing a feed patch size,

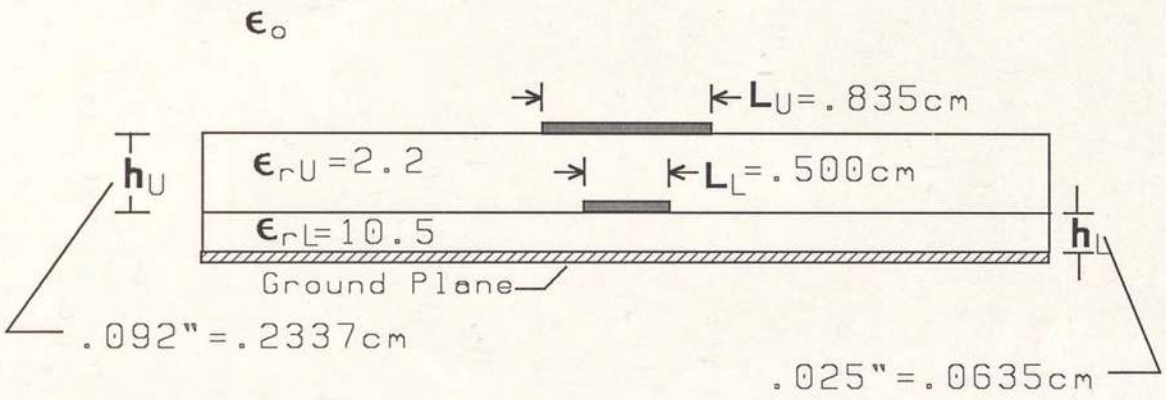

Figure 13(a). Two-Layer Microstrip Patch Antenna Element Configuration for Experimental Data of Figure 13.

$L_R = -20 \log \Gamma$

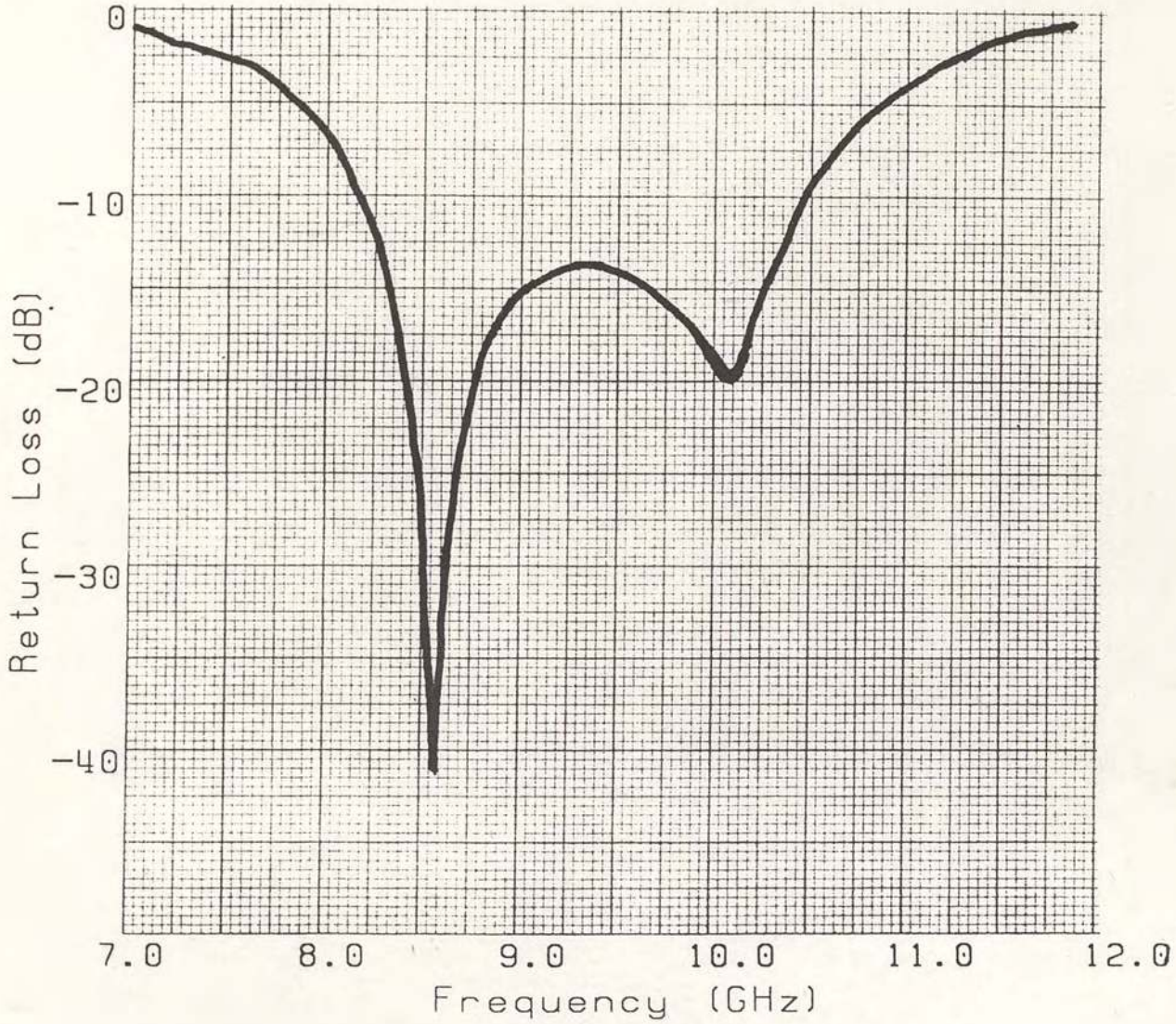

Figure 13(b). Return Loss for the Two-Layer Microstrip Patch Antenna Element Configuration of Figure 13(a).

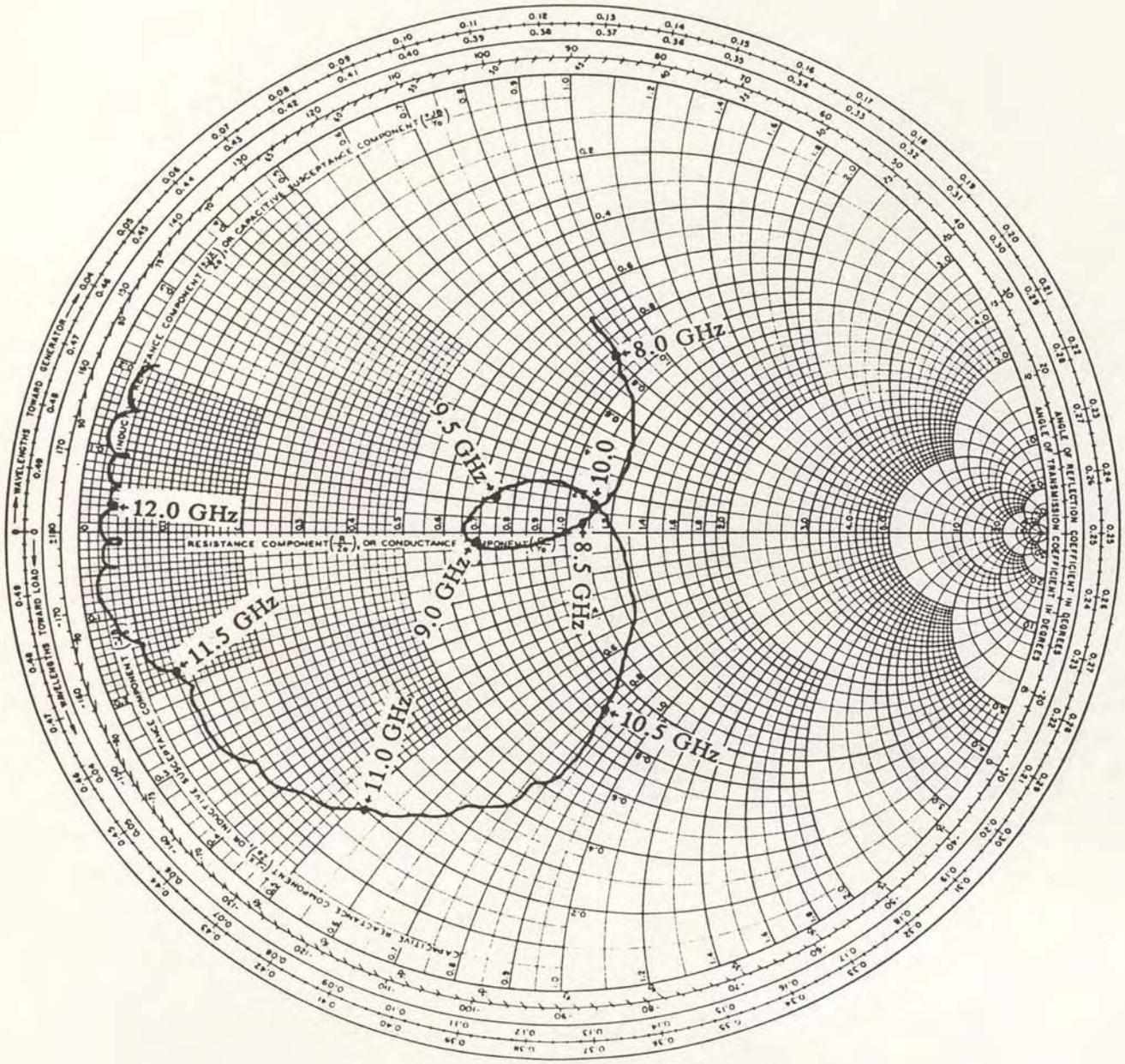

Figure 13(c). Smith Chart Over X Band for the Two-Layer Microstrip Patch Antenna Element Configuration of Figure 13(a).

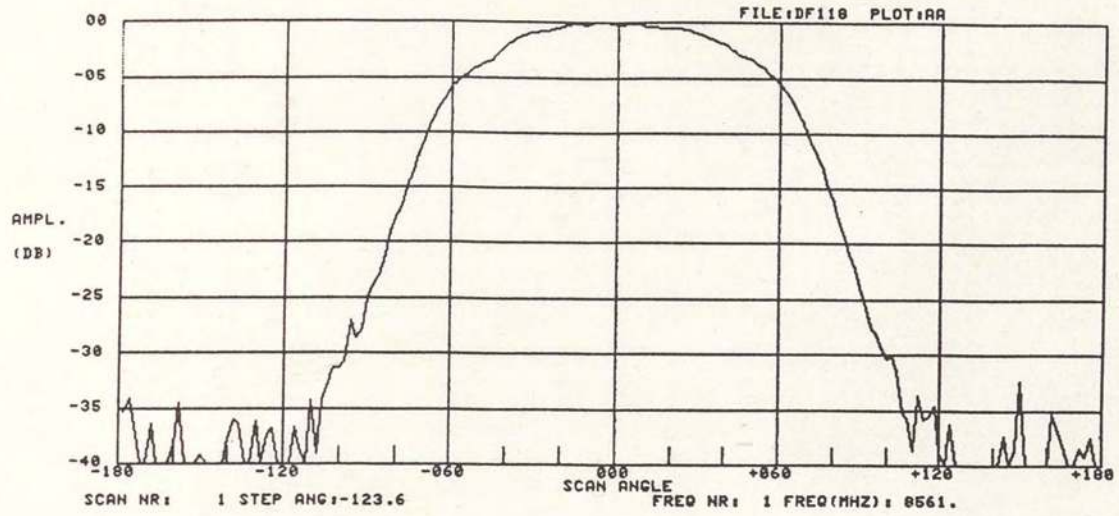

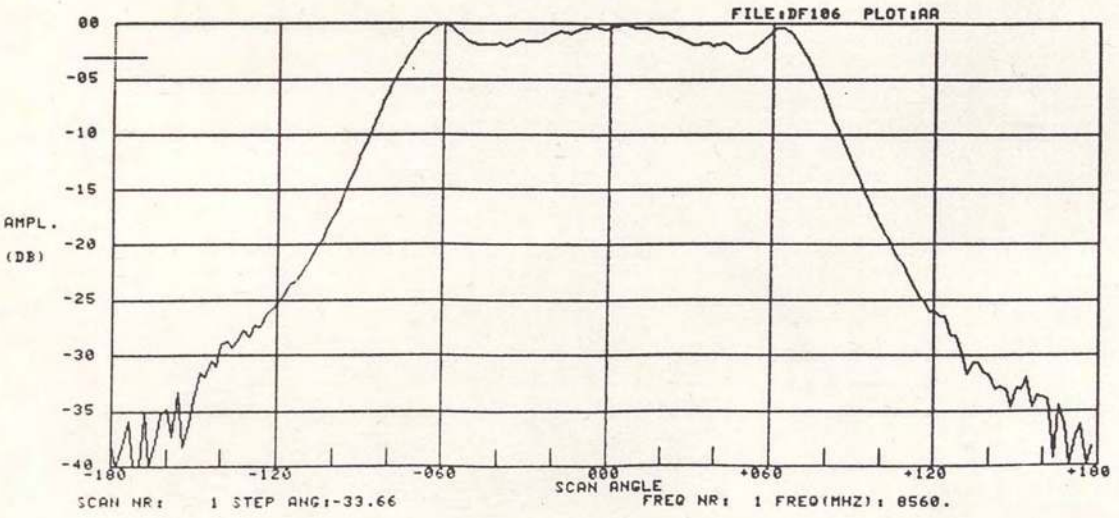

Figure 13(d). H-Plane (top) and E-Plane (bottom) at 8.56 GHz for the Two-Layer Microstrip Patch Antenna Element Configuration of Figure 13(a). (Gain=5.05dBi).

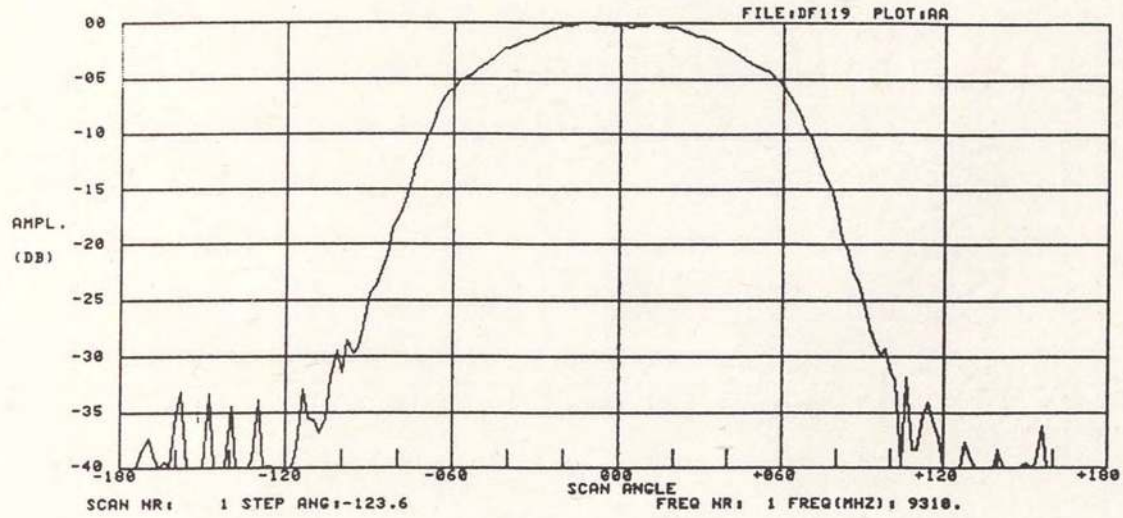

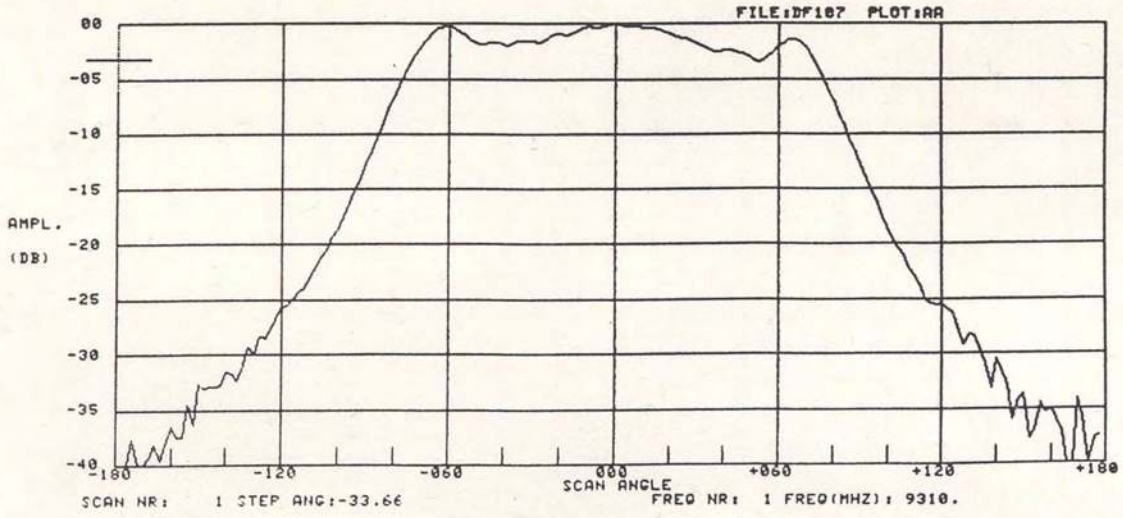

Figure 13(e). H-Plane (top) and E-Plane (bottom) at 9.31 GHz (Center Frequency Between Resonances) for the Two-Layer Microstrip Patch Antenna Element Configuration of Figure 13(a). (Gain=4.68dBi).

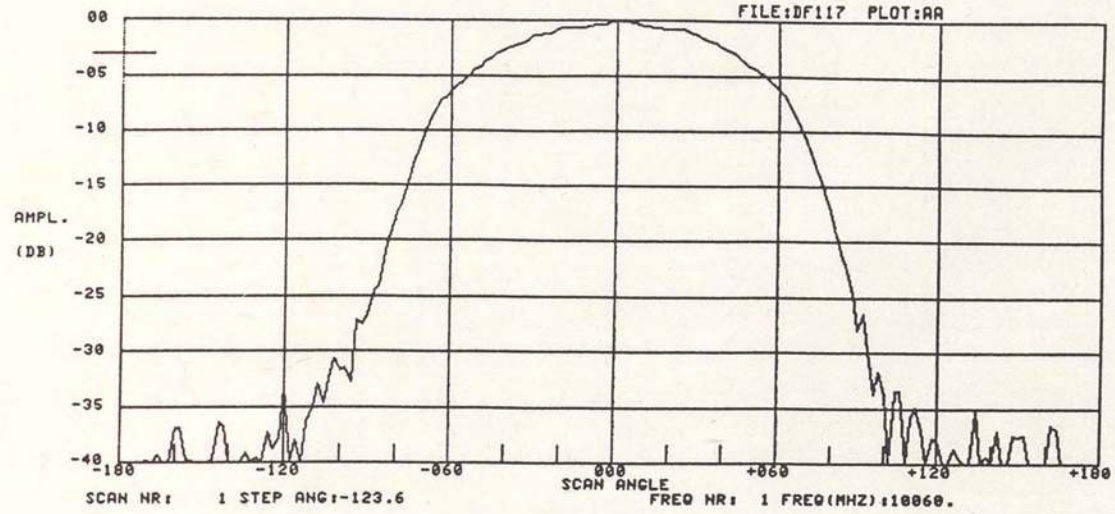

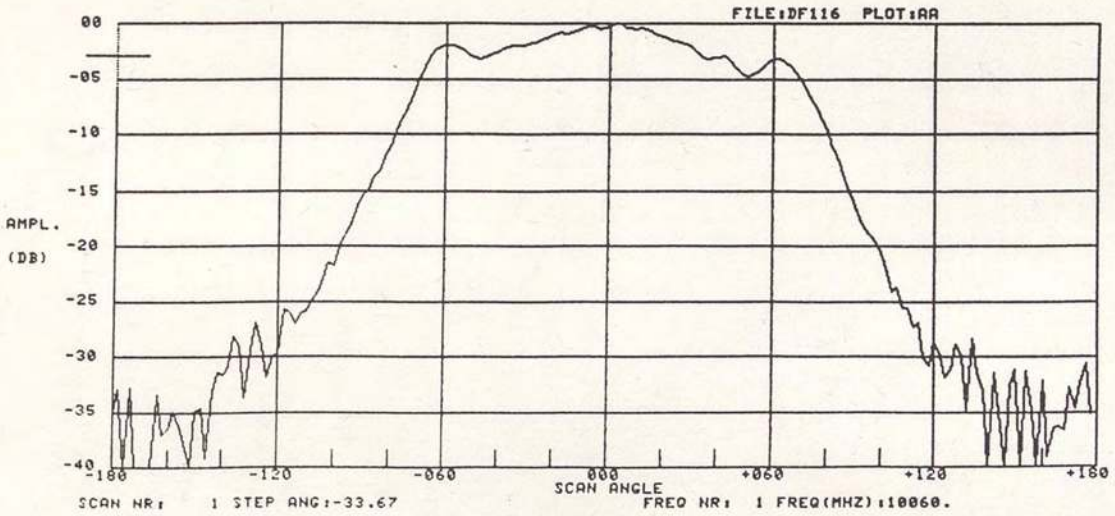

Figure 13(f). H–Plane (top) and E–Plane (bottom) at 10.06 GHz for the Two–Layer Microstrip Patch Antenna Element Configuration of Figure 13(a). (Gain=5.85dBi).

TABLE 3.
SUMMARY OF MEASURED AND PREDICTED RESULTS FOR THE TWO-LAYER MICROSTRIP PATCH ANTENNA ELEMENT OF FIGURE 13

	MEASURED	PREDICTED	%DIFF.	REMARKS
UPPER PATCH RESONANCE	8.56GHZ	9.2GHZ	7.0%	Eq. 3-20 or Figure 10(b).
LOWER PATCH RESONANCE	10.06GHZ	8.8GHZ	12.5%	Approx. from Figure 11(b).
2:1 VSWR FREQUENCY COVERAGE (<-9.54dB return loss)	8.14-10.46GHZ	-	-	
2:1 VSWR BANDWIDTH (% of center frequency)	24.9%	-	-	
@ 8.56 GHZ				
GAIN	5.05dBi	5.95dBi	18.7%	Gain prediction
H-PLANE HPBW*	89°	80°	11.3%	assumed 80%
E-PLANE HPBW	130°	100°	30.0%	efficiency.
@ f_c =9.31 GHZ	(same predictions as above)			Measured HPBW of
GAIN	4.68dBi			E-Plane
H-PLANE HPBW	90°			after
E-PLANE HPBW	130°			smoothing of plots.
@ 10.06 GHZ	(same predictions as above)			
GAIN	5.85dBi			
H-PLANE HPBW	87°			
E-PLANE HPBW	120°			

* HPBW is the half power beam width or width between the 3 dB down points of the radiation intensity pattern.

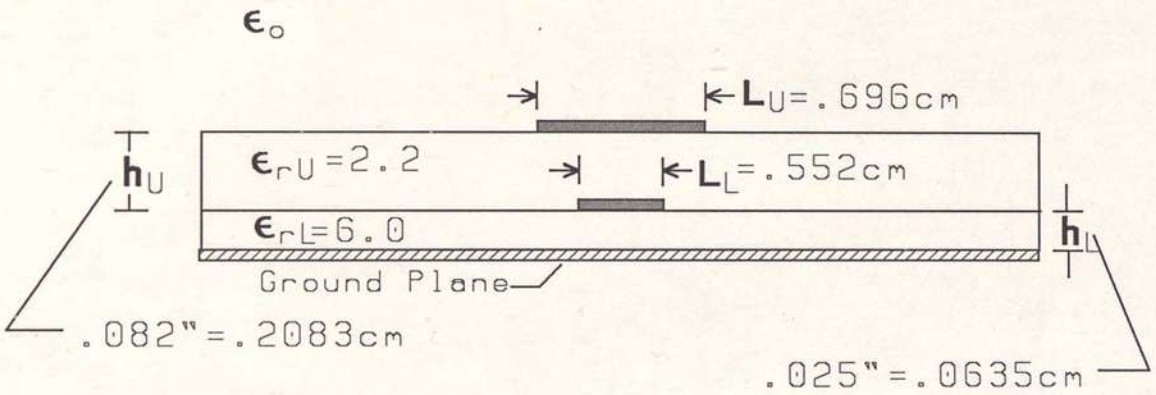

Figure 14(a). Two-Layer Microstrip Patch Antenna Element Configuration for Experimental Data of Figure 14.

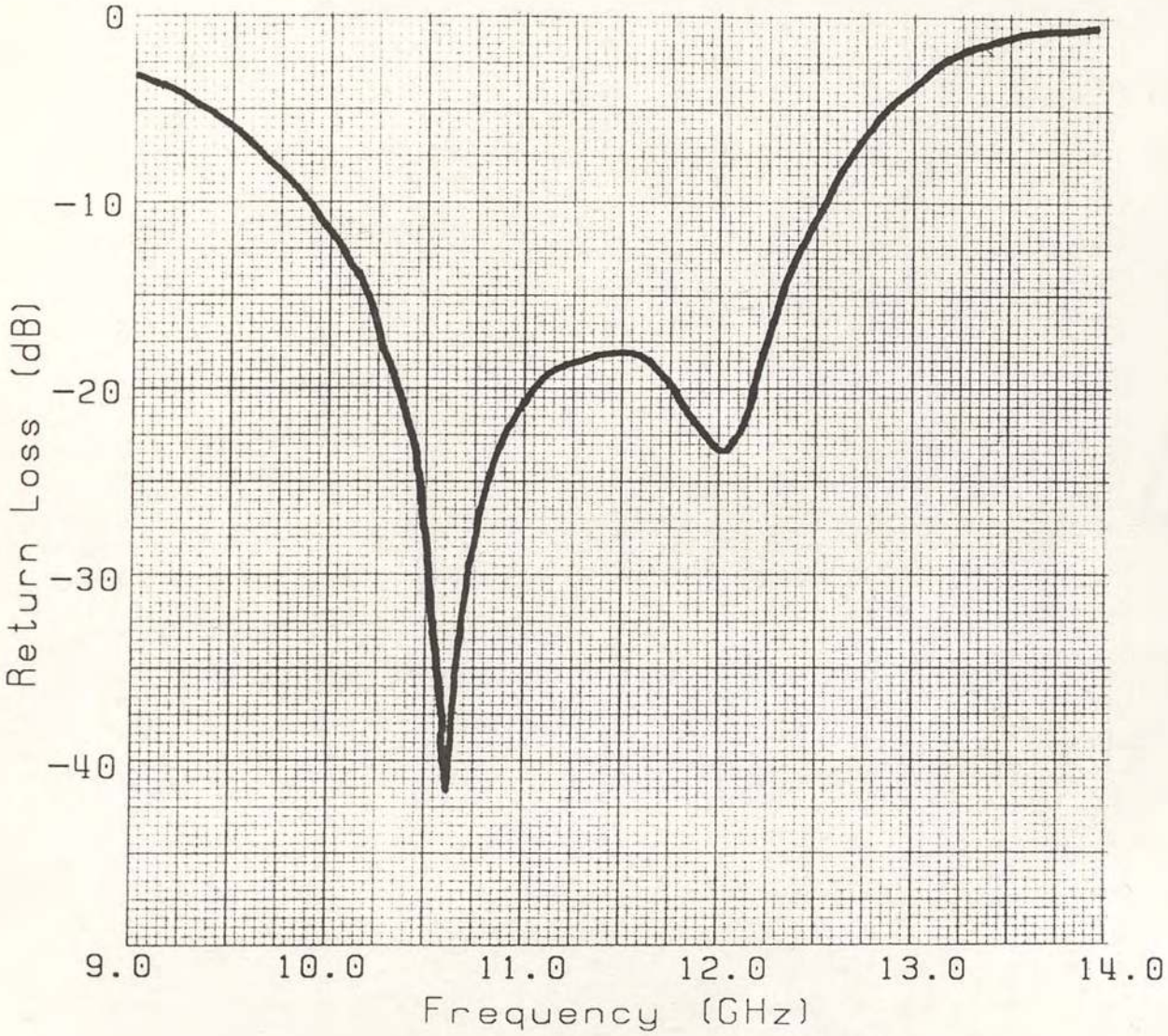

Figure 14(b). Return Loss for the Two-Layer Microstrip Patch Antenna Element Configuration of Figure 14(a).

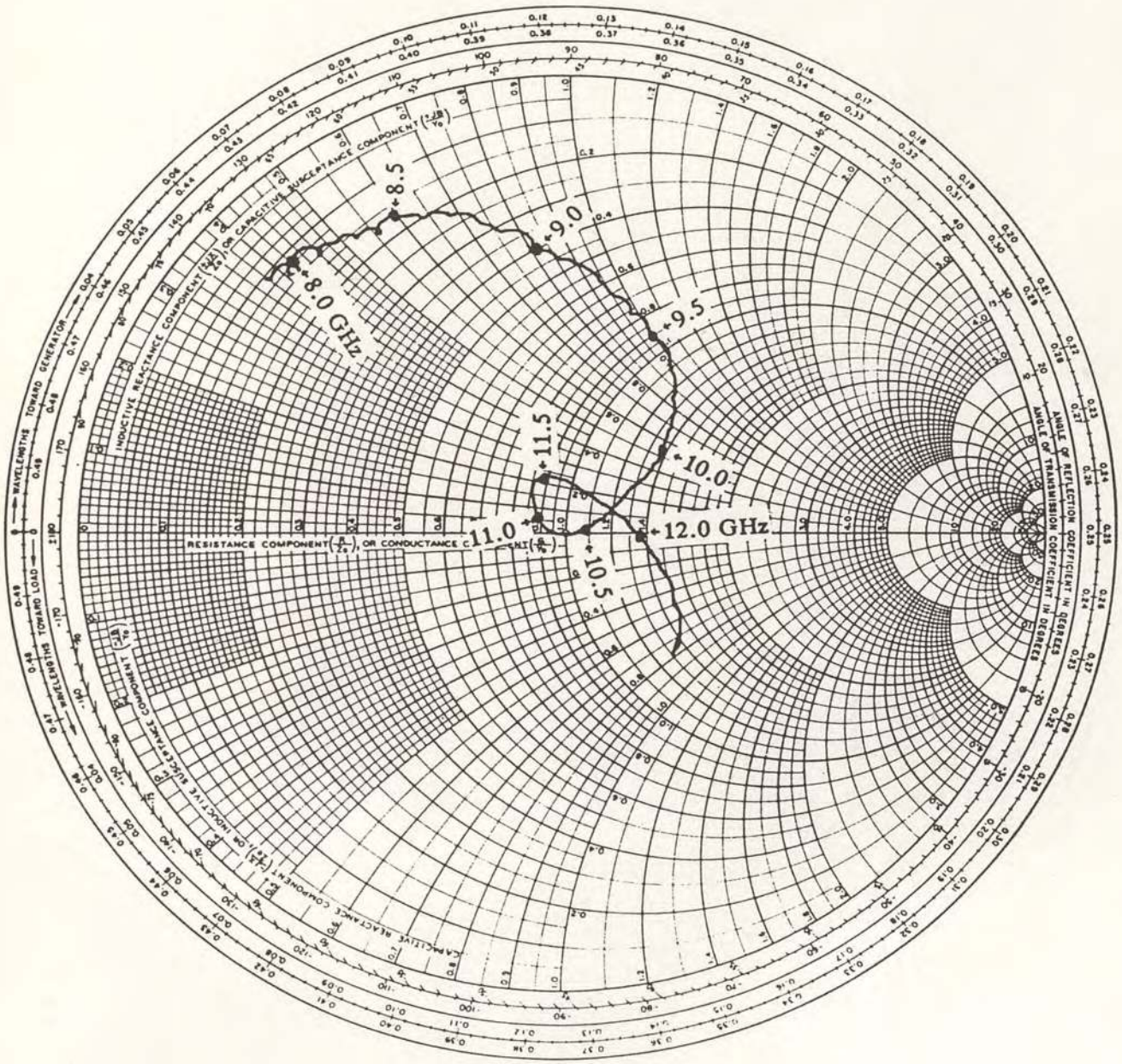

Figure 14(c). Smith Chart Over X Band for the Two-Layer Microstrip Patch Antenna Element Configuration of Figure 14(a).

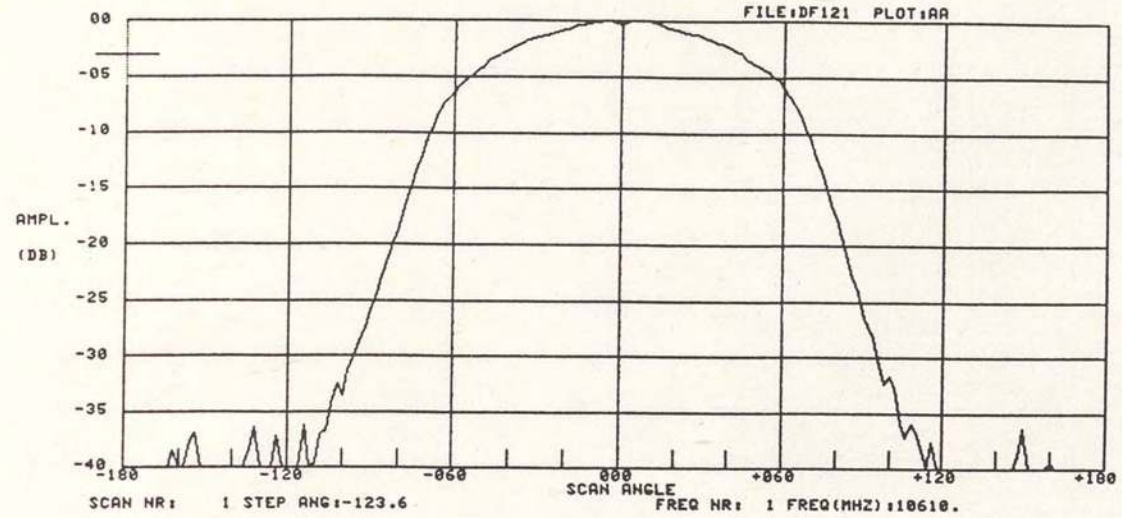

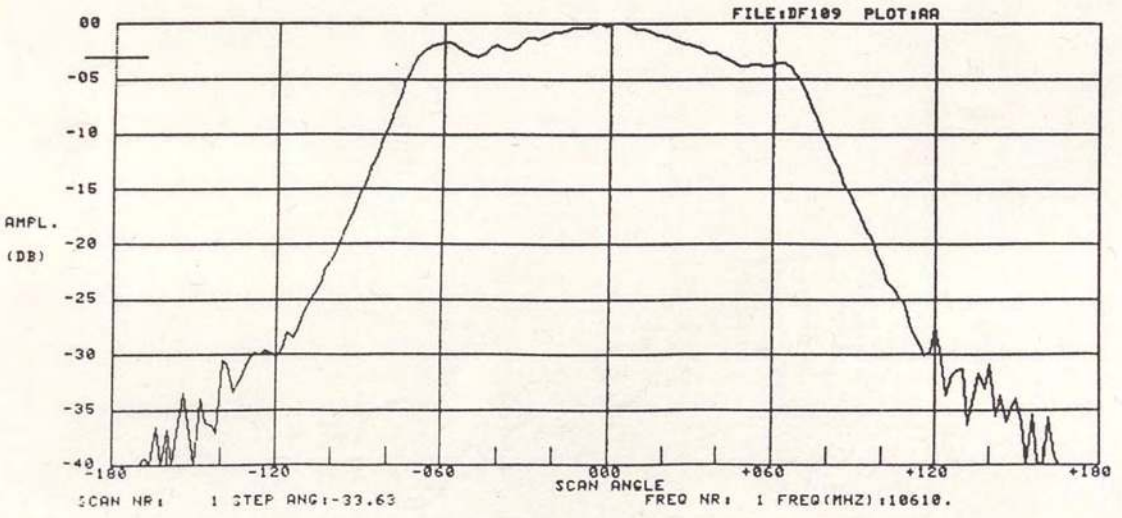

Figure 14(d). H-Plane (top) and E-Plane (bottom) at 10.61 GHz for the Two-Layer Microstrip Patch Antenna Element Configuration of Figure 14(a). (Gain=5.78dBi).

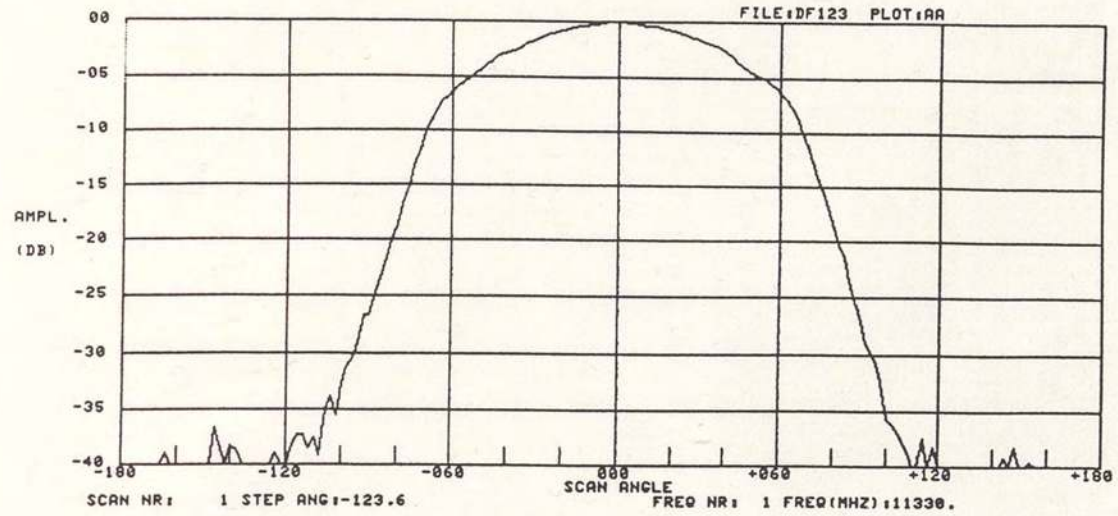

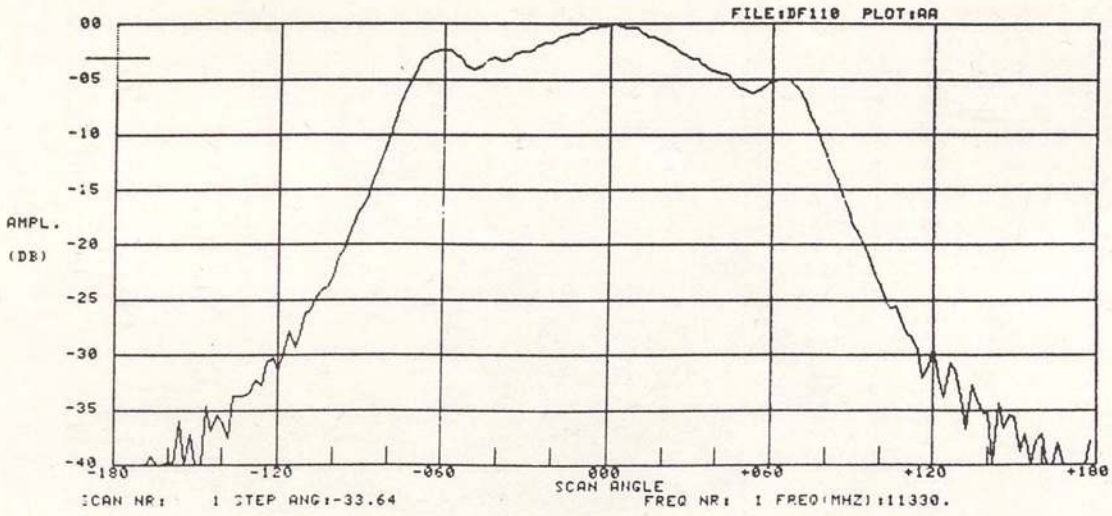

Figure 14(e). H-Plane (top) and E-Plane (bottom) at 11.33 GHz (Center Frequency Between Resonances) for the Two-Layer Microstrip Patch Antenna Element Configuration of Figure 14(a). (Gain=6.88dBi).

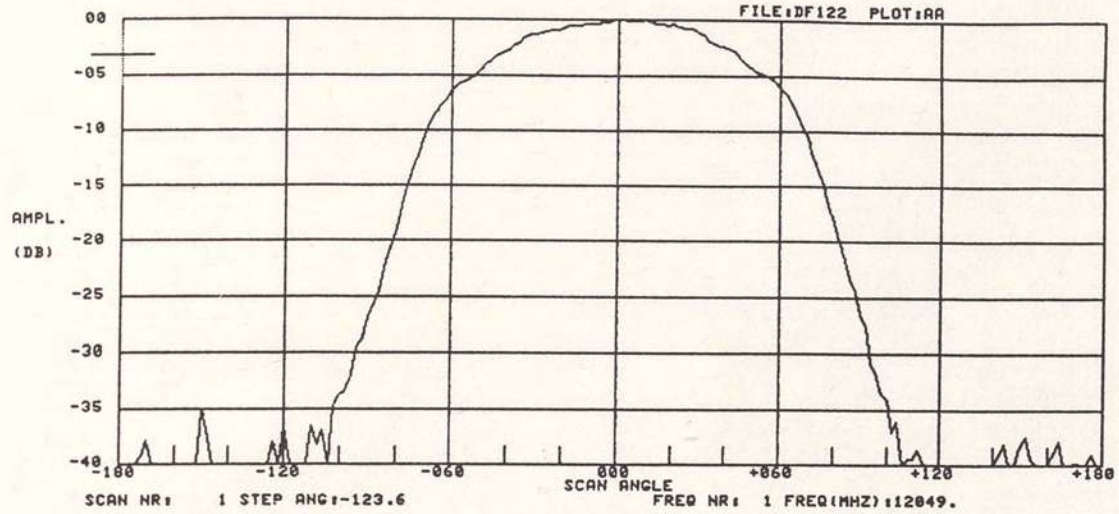

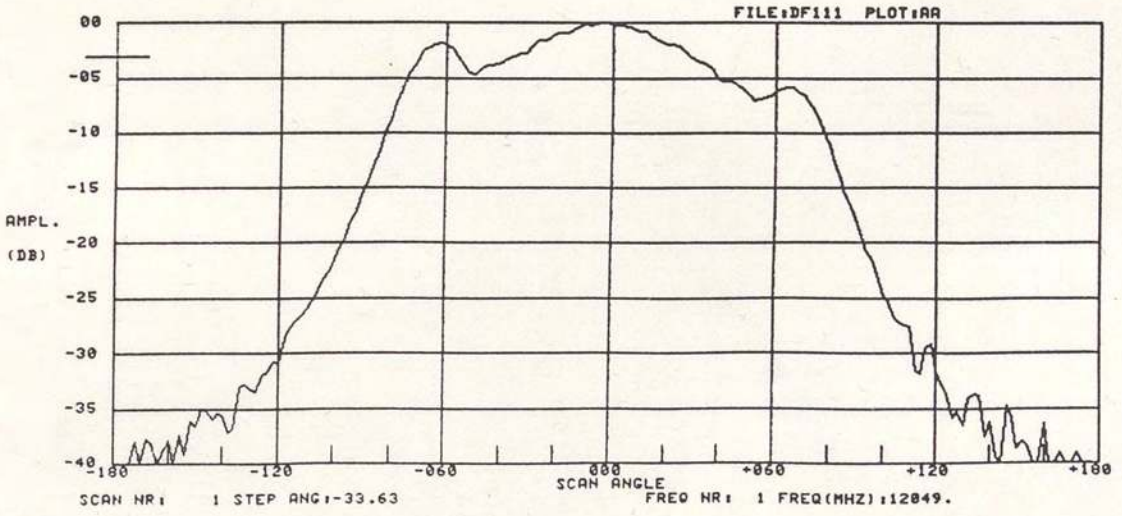

Figure 14(f). H–Plane (top) and E–Plane (bottom) at 12.05 GHz for the Two–Layer Microstrip Patch Antenna Element Configuration of Figure 14(a). (Gain=6.80dBi).

TABLE 4.
SUMMARY OF MEASURED AND PREDICTED RESULTS FOR THE TWO-LAYER MICROSTRIP PATCH ANTENNA ELEMENT OF FIGURE 14

	MEASURED	PREDICTED	%DIFF.	REMARKS
UPPER PATCH RESONANCE	10.61GHZ	10.85GHZ	2.3%	Eq. 3-20 or Figure 10(c).
LOWER PATCH RESONANCE	12.05GHZ	10.50GHZ	14.8%	Approx. from Figure 11(c).
2:1 VSWR FREQUENCY COVERAGE (<-9.54dB return loss)	9.85-12.55GHZ	-	-	
2:1 VSWR BANDWIDTH (% of center frequency)	23.83%	-	-	
@ 10.61 GHZ				
GAIN	5.78dBi	5.90dBi	2.8%	Gain prediction
H-PLANE HPBW	88°	80°	10.0%	assumed 80%
E-PLANE HPBW	130°	100°	30.0%	efficiency. Measured
@ f_c =11.33 GHZ	(Same predictions as above)			HPBW
GAIN	6.88dBi			after
H-PLANE HPBW	84°			smoothing
E-PLANE HPBW	125°			of plots.
@ 12.05 GHZ	(Same predictions as above)			
GAIN	6.80dBi			
H-PLANE HPBW	85°			
E-PLANE HPBW	120°			

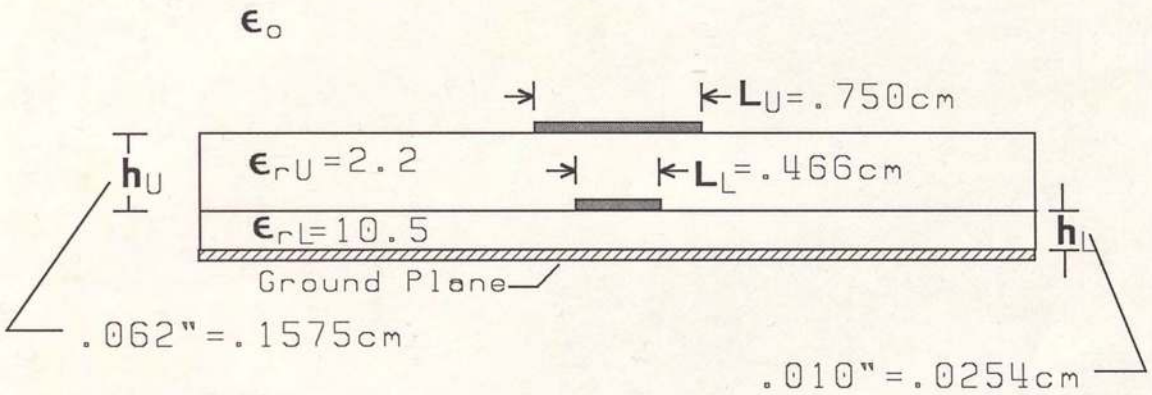

Figure 15(a). Two-Layer Microstrip Patch Antenna Element Configuration for Experimental Data of Figure 15.

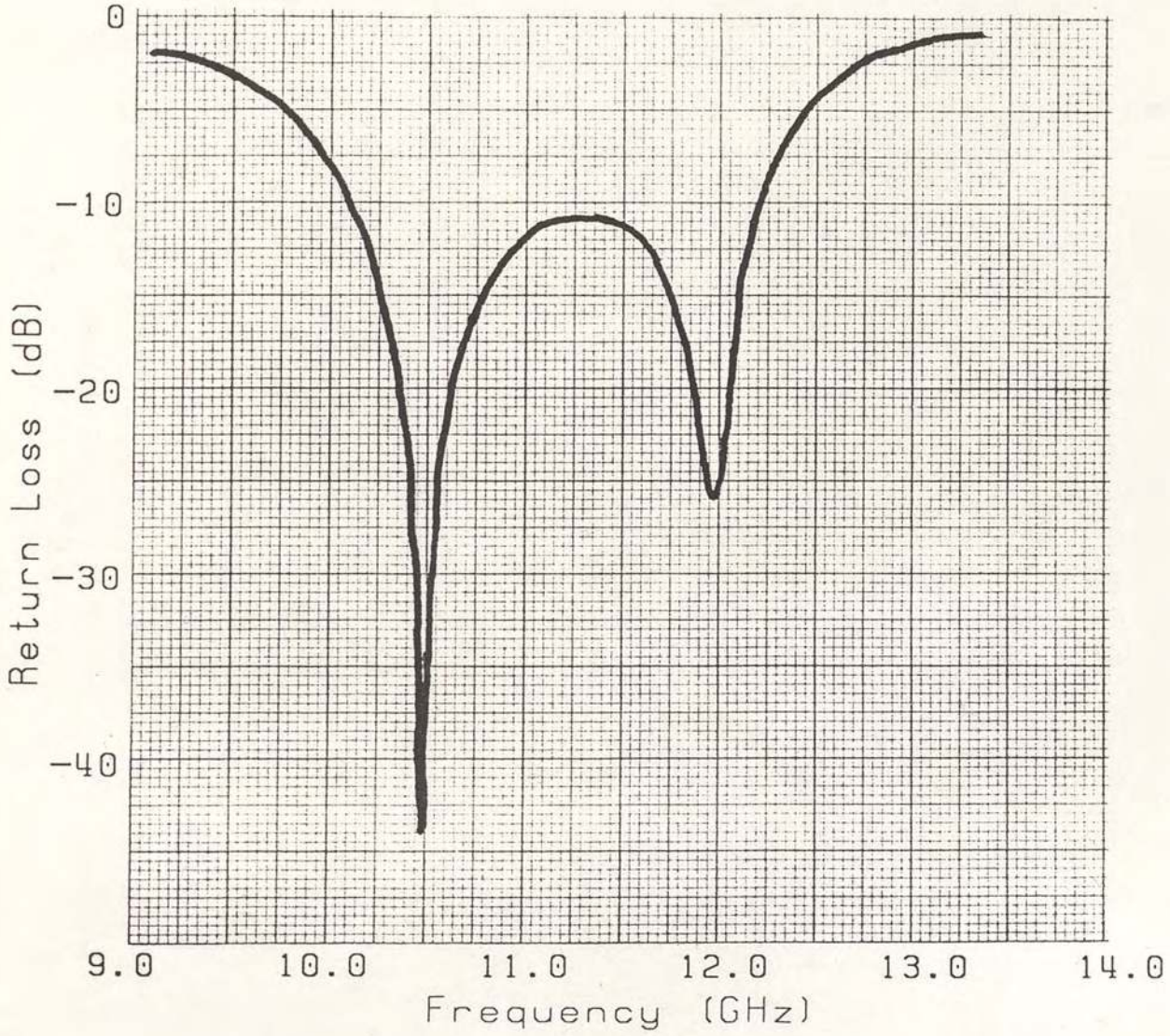

Figure 15(b). Return Loss for the Two-Layer Microstrip Patch Antenna Element Configuration of Figure 15(a).

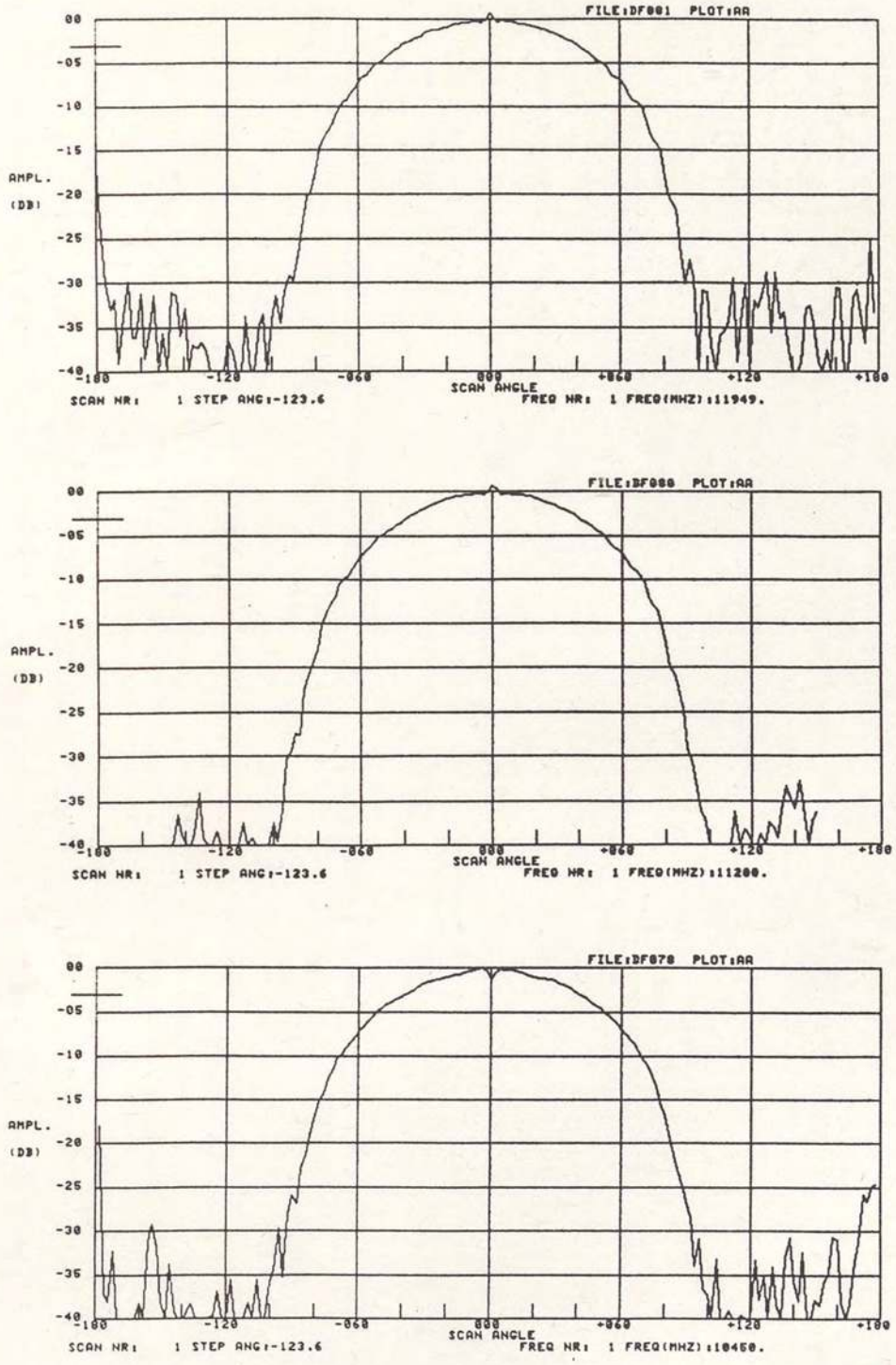

Figure 15(c). H–Plane at 11.95 GHz (top), 11.20 GHz (middle) and 10.45 GHz (bottom) for the Two–Layer Microstrip Patch Antenna Element Configuration of Figure 15(a).

TABLE 5.
SUMMARY OF MEASURED AND PREDICTED RESULTS FOR THE TWO-LAYER MICROSTRIP PATCH ANTENNA ELEMENT OF FIGURE 15

	MEASURED	PREDICTED	%DIFF.	REMARKS
UPPER PATCH RESONANCE	10.45GHZ	11.20GHZ	6.7%	Eq. 3-20 or Figure 10(a).
LOWER PATCH RESONANCE	11.95GHZ	9.8GHZ	21.9%	Approx. from Figure 11(a).
2:1 VSWR FREQUENCY COVERAGE (<-9.54dB return loss)	10.10-12.23GHZ	-	-	
2:1 VSWR BANDWIDTH (% of center frequency)	19.16%	-	-	
@ 10.45 GHZ H-PLANE HPBW	80°	80°	0.0%	
@ f_c =11.20 GHZ H-PLANE HPBW	80°	(Same prediction as above)		
@ 11.95 GHZ H-PLANE HPBW	80°	(Same prediction as above)		

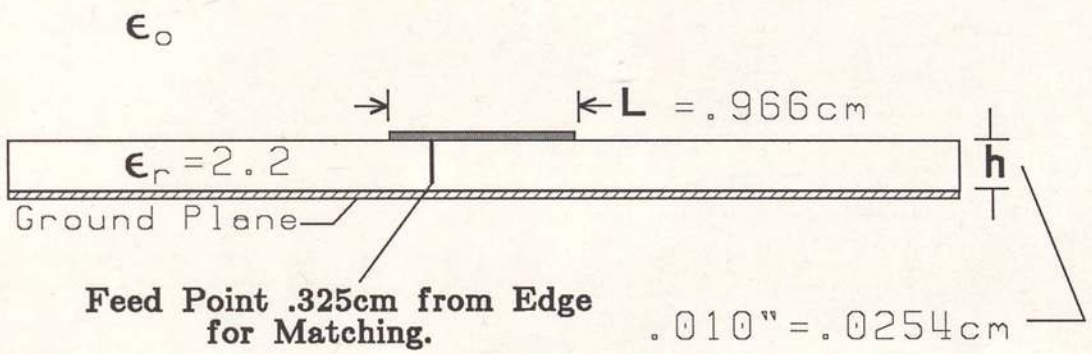

Figure 16(a). Single Layer Microstrip Patch Antenna Element Configuration for Experimental Data of Figure 16.

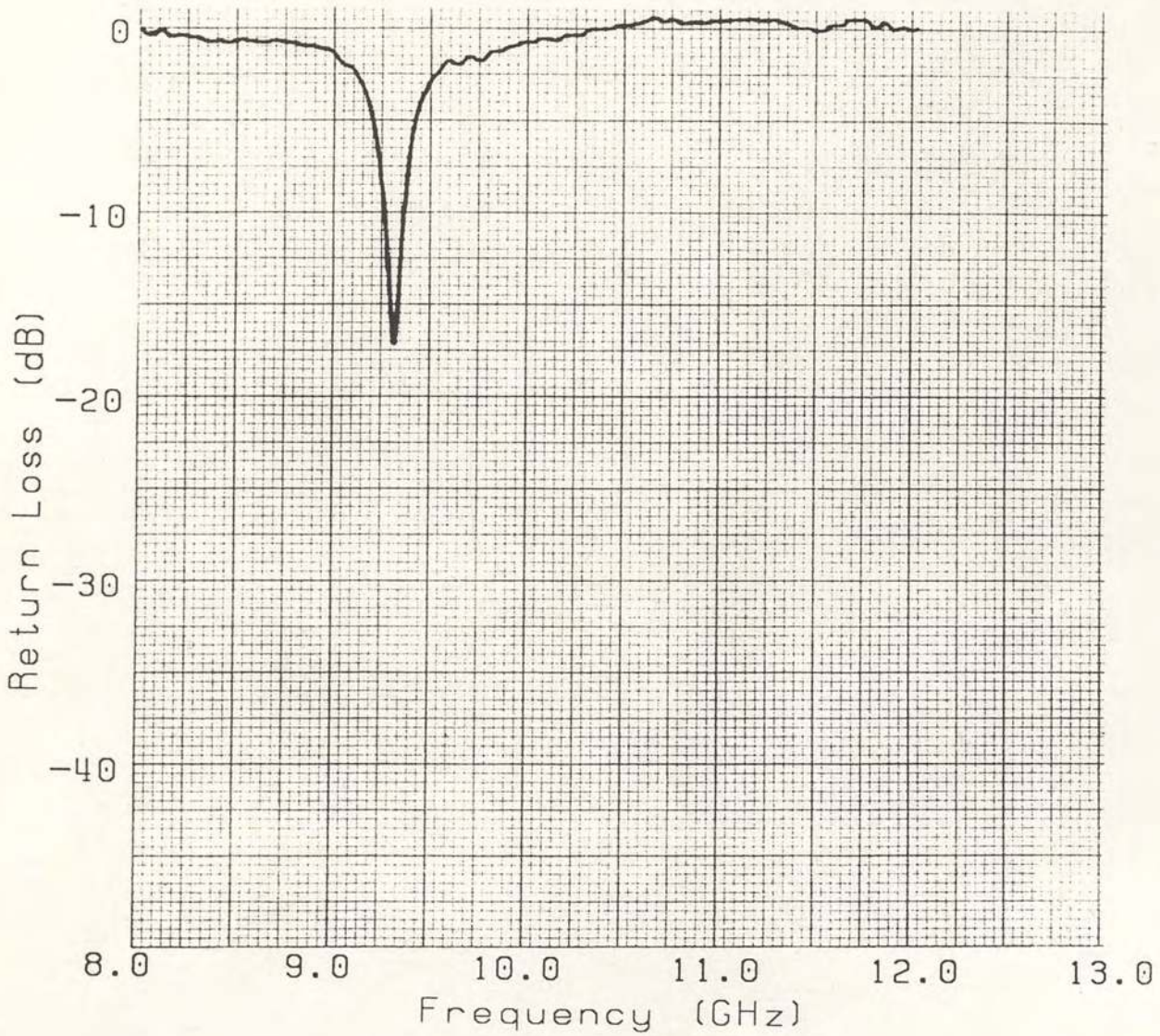

Figure 16(b). Return Loss for the Single Layer Microstrip Patch Antenna Element Configuration of Figure 16(a).

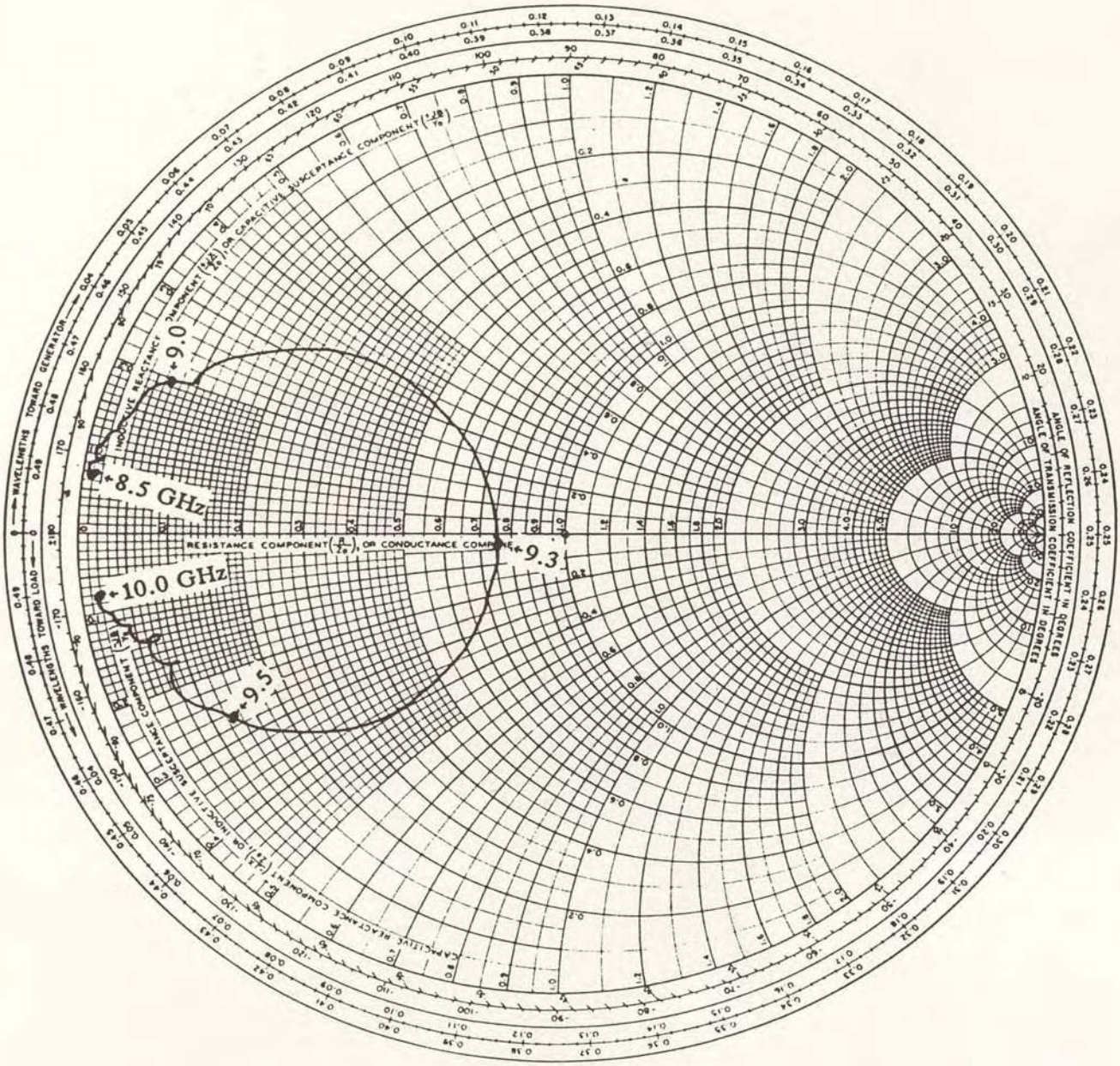

Figure 16(c). Smith Chart Over X Band for the Single Layer Microstrip Patch Antenna Element Configuration of Figure 16(a).

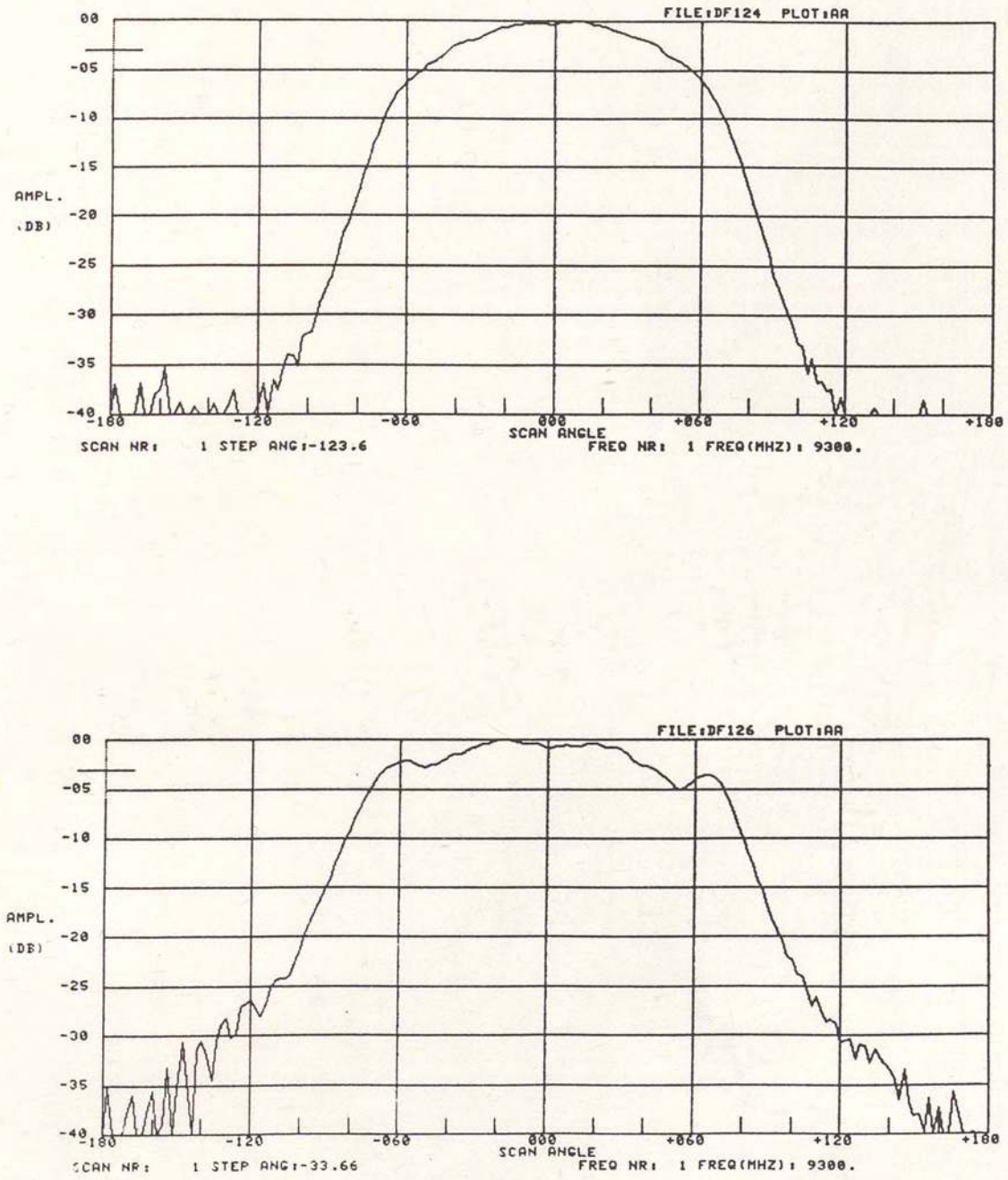

Figure 16(d). H–Plane (top) and E–Plane (bottom) at 9.30 GHz for the Single Layer Microstrip Patch Antenna Element Configuration of Figure 16(a). (Gain=4.56dBi).

TABLE 6.
SUMMARY OF MEASURED RESULTS FOR THE
SINGLE LAYER MICROSTRIP PATCH ANTENNA ELEMENT
OF FIGURE 16

	MEASURED
PATCH RESONANCE	9.30 GHZ
2:1 VSWR FREQUENCY COVERAGE (<−9.54dB return loss)	9.25–9.32 GHZ
2:1 VSWR BANDWIDTH (% of center frequency)	0.75%
@ 9.30 GHZ	
GAIN	4.56dBi
H–PLANE HPBW	87°
E–PLANE HPBW	120°

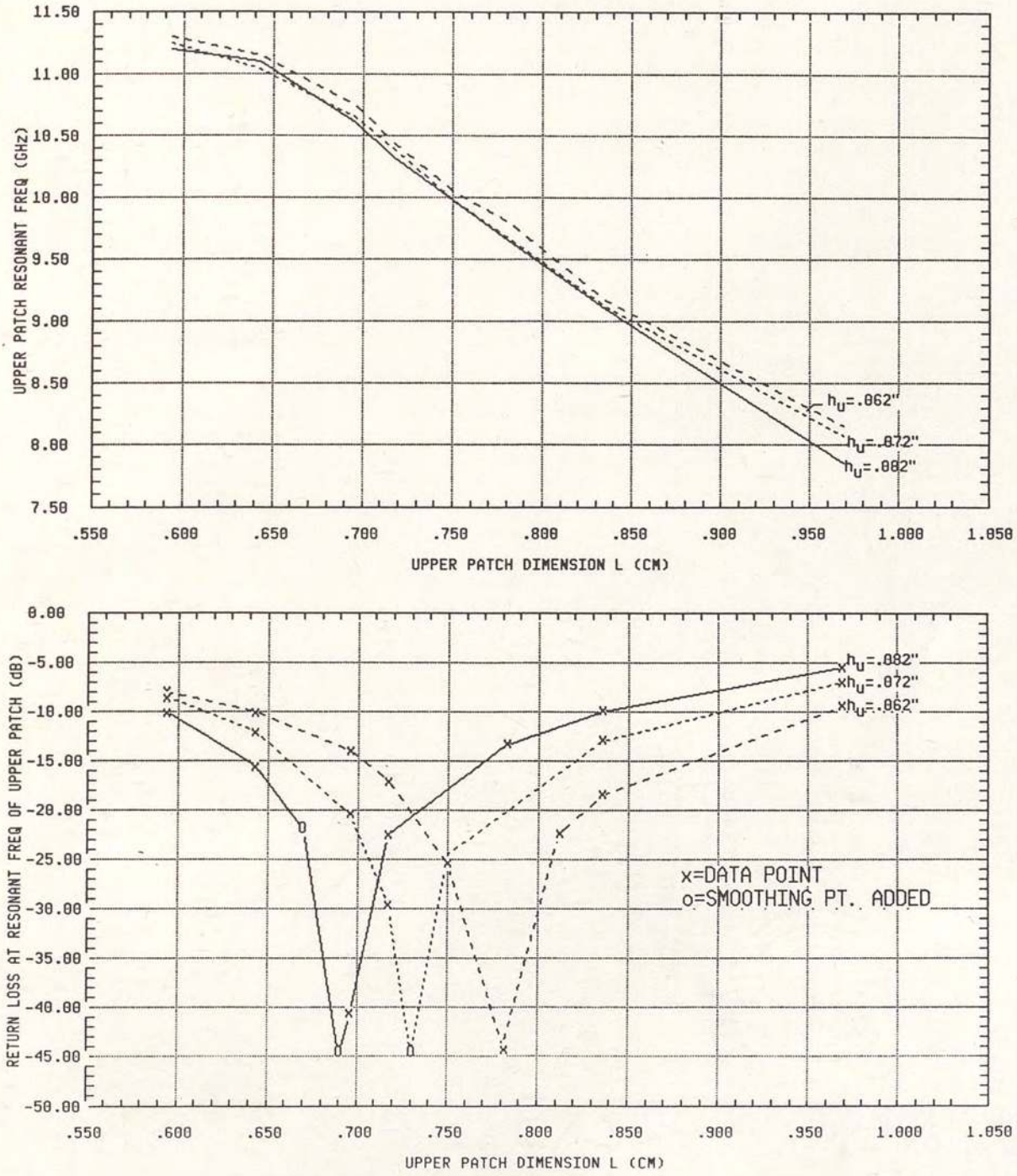

Figure 17(a). Frequency (top) and Return Loss (bottom) at Upper Patch Resonance as a Function of Upper Patch Length for the Two-Layer Microstrip Patch Antenna Element with $\epsilon_{rL}=6$, $h_L=.025''$, $L_L=.552cm=.2173''$, $\epsilon_{ru}=2.2$, and hu as shown.

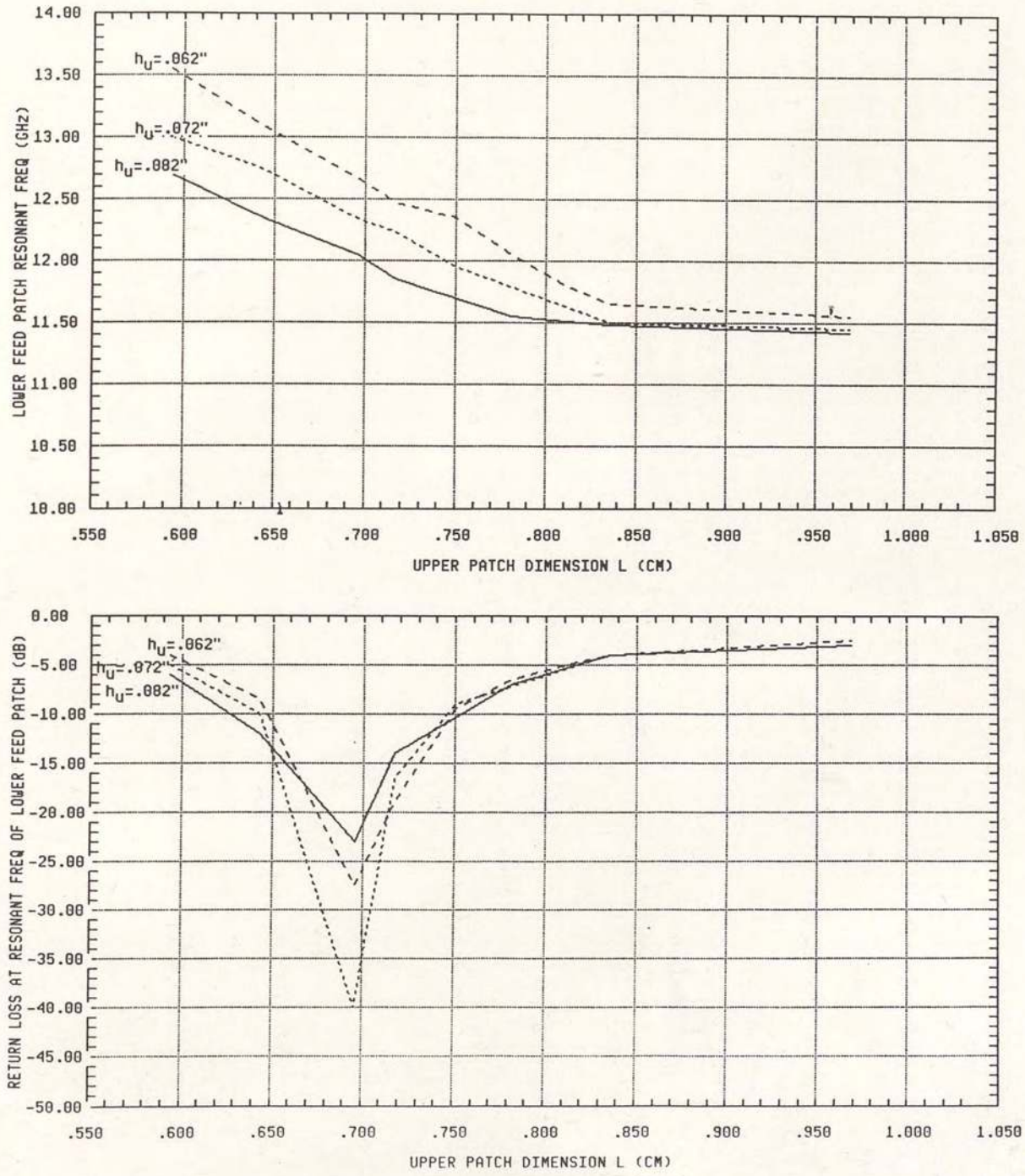

Figure 17(b). Frequency (top) and Return Loss (bottom) at Lower Patch Resonance as a Function of Upper Patch Length for the Two-Layer Microstrip Patch Antenna Element with ϵ_{rL}=6, h_L=.025", L_L=.552cm=.2173", ϵ_{ru}=2.2, and hu as shown.

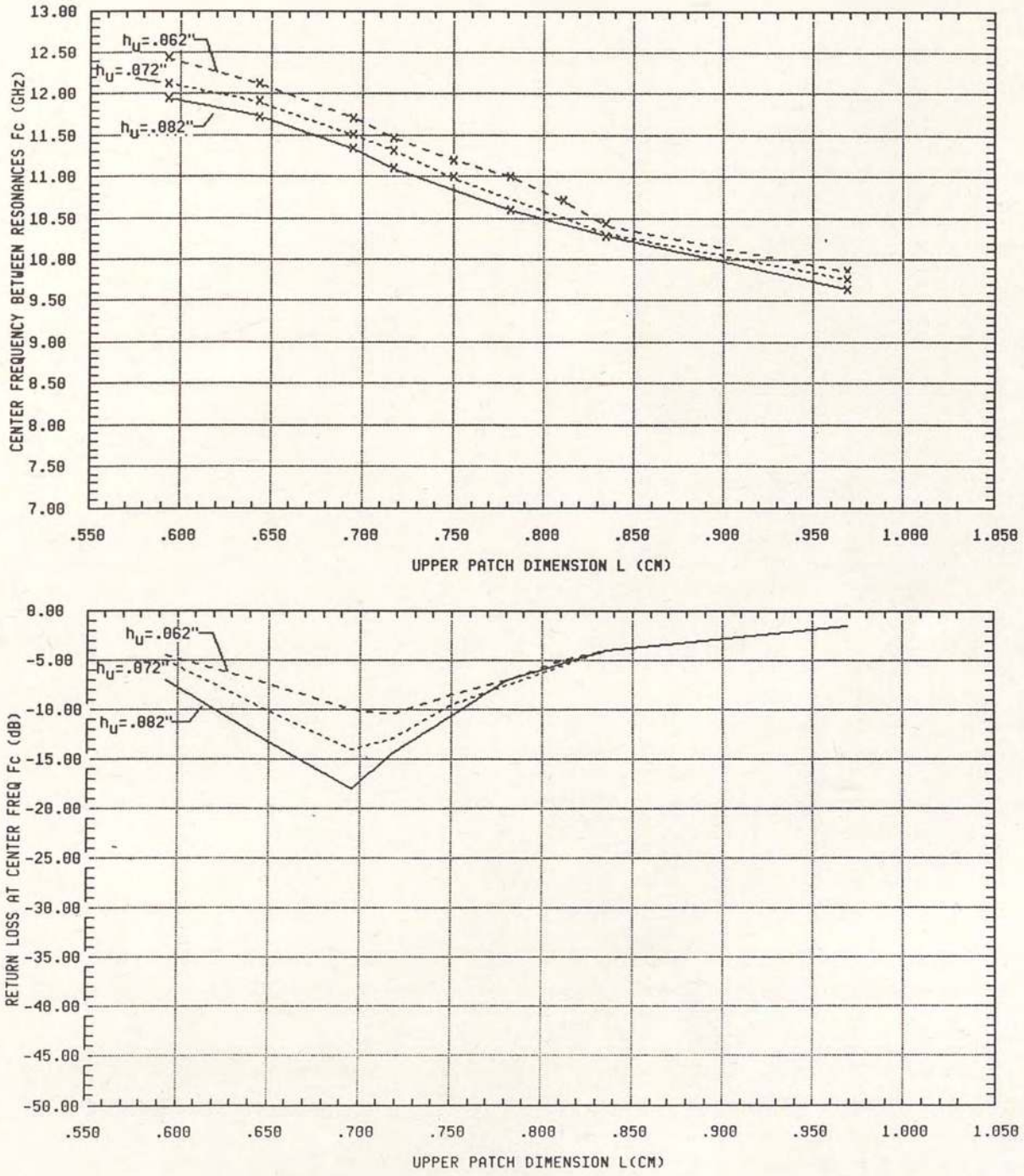

Figure 17(c). Center Frequency Between Resonances (top) and Return Loss at f_c (bottom) as a Function of Upper Patch Length for the Two-Layer Microstrip Patch Antenna Element with $\epsilon_{rL}=6$, $h_L=.025''$, $L_L=.552cm=.2173''$, $\epsilon_{ru}=2.2$, and hu as shown.

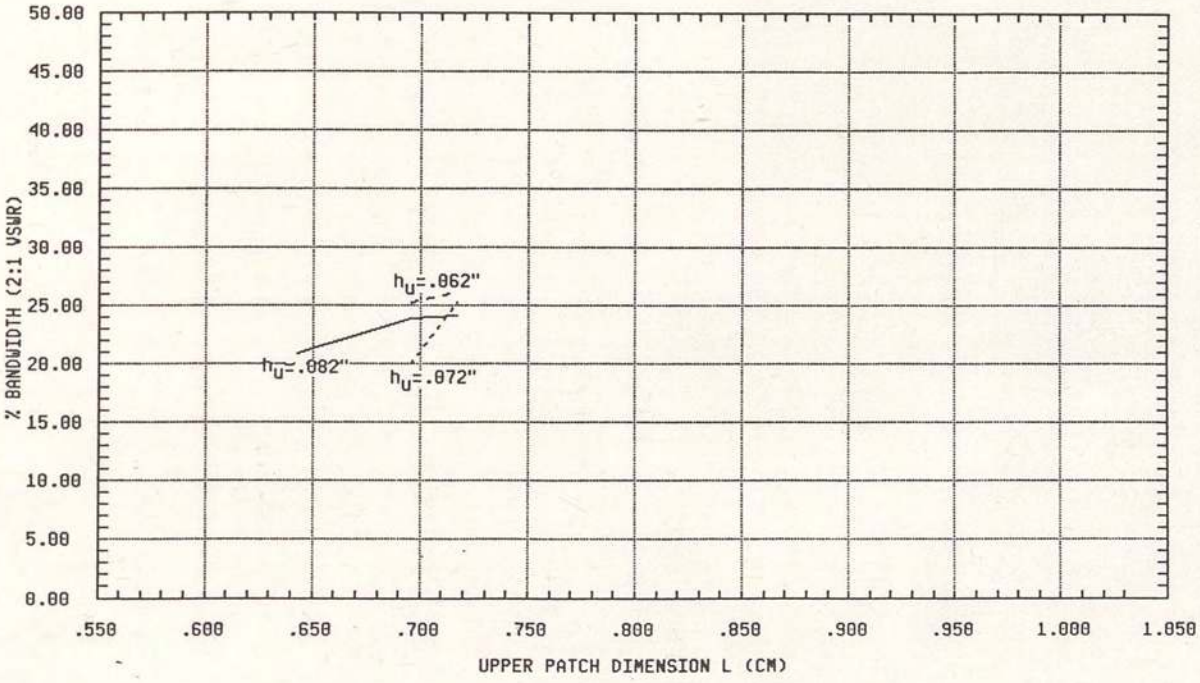

Figure 17(d). Bandwidth (% of f_c) as a Function of Upper Patch Length for the Two-Layer Microstrip Patch Antenna Element with ϵ_{rL}=6, h_L=.025", L_L=.552cm=.2173", ϵ_{ru}=2.2, and hu as shown.

combining it with the many upper feed elements and observing the return loss response. Upper dielectric heights other than the standard were obtained with dielectric spacers of .010″ or .020″. Many configurations did not work, being poorly matched, or showing only one resonance (upper patch resonance) or having dual resonances spread too far apart (like a dual frequency antenna). Through this combining, definite patterns for resonant frequency and matching began to become apparent which aided the pinpointing of working configurations. More will be said on this in the discussion of Figure 17.

The (a) part of figures 13–16 graphically depicts the patch element configuration for the experimental data of that figure. Part (b) is the return loss* for the element. Note the expected dual resonances of the two–layer designs. It is easily seen how greatly the bandwith of the patch element was increased by comparing figures 13(b), 14(b), and 15(b) to the single layer patch return loss response of Figure 16(b). The two–layer element bandwidths are on the order of 20% while the single layer patch bandwidth is on the order of 1% (see data summary tables 3, 4, 5 and 6 for exact calculations). For the dual resonance responses, the lower resonance, in frequency, was always found to be due to the upper patch. This was known since changes in the upper patch size predominantly affected this resonance.

---

*Return loss (S_{11}) data was recorded using an HP8410 or a Wavetek 1038 network analyzer (characteristic impedance $Z_o = 50\Omega$).

Several attempts were made to "pass" the resonances by each other (using upper feed patches of smaller length), but all were unsuccessful. The upper patch resonance is better matched than the lower patch resonance in the responses shown, but this was not always the case. As seen in the data summary tables 3, 4, and 5, the prediction of the upper patch resonance was good, within 7% in all three cases. This indicates that coupling between the patches is not a major factor in determining the resonance of the upper patch, since coupling was neglected in the prediction. The lower feed patch resonant frequency prediction was not as successful, missing the actual by 12 to 22%. Coupling, as well as effective dielectric and patch size must play a substantial part in determining the lower patch resonance.

The (b) part of figures 13, 14 and 16 is the measured impedance Smith Chart data for the element of that figure taken with an HP8410 network analyzer. The broadband response of the two-layer design is seen in the tight loop around the center of the chart, while the single layer patch makes one quick pass (quick over frequency) near the center of the chart. Very little, if any, inductive shift was seen in the charts.

The (d), (e), and (f) parts of figures 13 and 14 show the measured H and E-plane radiation intensity patterns at three frequencies across the band of each element (at the lower resonance frequency, the center frequency between resonances, and the upper resonance frequency). Figure 15(c) is H-plane cuts for that two-layer element. Figure 16(d) shows the single layer patch H and E-plane patterns at its resonant frequency. The patterns

were taken with the element on a 2 feet diameter, circular ground plane, placed in an anechoic chamber. A Scietific Atlanta SA2020 was used to collect and plot the data. A thin piece of absorber was placed on the outer edge of the ground plane to muffle edge diffraction interference. Some interference can still be seen in the E-plane patterns (for both the single and two-layer configurations) causing an extra ripple around ±60°. The presence of the aberration in the patterns of both the single and two-layer antenna elements indicates that it is not due to the element stacking. The nearly identical H-plane and nearly identical E-plane radiation patterns of the two-layer designs to the single layer design show that broadbanding was achieved without detrimental effects to the radiation pattern of the elements. The similar gains, on the order of 5 dBi measured by referencing to a standard gain horn, of the two-layer and single layer elements indicate that efficiency was maintained in the broadband design. Similar patterns and gain over the bandwidth of the two-layer antenna elements show that the radiation pattern is not frequency dependant (within the band of the antenna). The H-plane patterns were all very similar to the theoretical predictions (Figures 6 and 7), with HPBWs (half power or 3 dB down beam widths) between 80° and 90°. The E-plane HPBWs (measured after smoothing of the pattern) were between 120 and 130°, slightly higher than expected (Figure 7), but showing clearly that, as predicted, the radiation is primarily effected by the low dielectric of the upper patch, which keeps the

HPBW low (compared to the theoretical higher dielectric patterns of Figure 6(a)). Several cross polarization patterns taken were consistent and indicated a cross polarization rejection greater than about 17 dB. Tables 3, 4, 5 and 6 give a summary of measured and predicted results for the antenna elements of figures 13, 14, 15 and 16, respectively.

Figure 17 displays typical measured frequency, return loss, and bandwidth information for one specific feed patch (ϵ_{rL}=6, h_L=.025″, L=.552cm= .2173″), with variables of upper patch length dimension (L) and upper patch dielectric height (h_L). The top of Figure 17(a) shows measured upper patch resonant frequency and was, on average, approximately 3% lower than the theoretical prediction displayed in Figure 10(c). The flattening of the curve on the lower end of the x axis, as the upper patch size approaches the lower patch size, was seen to occur for other feeds as well and seems to be a maximum frequency condition of the coupling. Poor return loss was also seen in this area. As a plausible explanation, consider that if the upper patch were made smaller than the feed patch, then the radiation from the feed patch edges would not be directly under the upper patch, the coupling would be very weak, yielding no excitation of the upper patch. The bottom graph of Figure 17(a) is of return loss measured at the upper patch resonant frequency. The pattern seen in this data gives some proof to the previous speculation that virtually any patch resonance could be matched by adjusting the dielectric height. Note that as the dielectric height

was increased, the best matched patch size and thus resonant wavelength decreased (best matched frequency increased). This was repeated in the data of the $\epsilon_{rL}=10.5$ feed patches and seems to be backward from what was logically expected. Therefore, a constant ratio of upper patch resonant wavelength to upper dielectric height for best matching (feed patch remaining constant) must not be the case. The top graph of Figure 17(b) is the lower feed patch resonant frequency versus the upper patch size. If effective dielectric and lower patch length were the only factors involved here, this plot would be horizontal lines, since the feed remained unchanged. Coupling is a substantial factor and seems to "push" the lower patch resonant frequency higher as the upper patch size decreases. From the bottom of Figure 17(b) it can be seen that the best match point for the lower feed resonance occurs at roughly the same upper patch size, but at different frequencies. Figure 17(c) shows the center frequency between resonances and return loss at this frequency as the upper patch size is varied. Broadbanding was obtained only where the center frequency return loss was less than −9.54dB, to form continuous 2:1 VSWR band coverage across both resonances. Figure 17(d) shows percent bandwidth over the area where broadbanding was achieved. The bandwidth for the combinations of this feed ranged from 20.0% to 26.1%.

The family curve patterns of Figure 17 were seen, as well, when combining other feed elements with various upper patches. These curves can

be used to pick out the best matched across the band, or the broadest band element configuration for that particular feed patch and determine its frequency coverage. Scaling could then be used to shift to a desired frquency range. More suggestions on this are given in the next section.

The experimental results examined in this section demonstrate that a practical broadband microstrip antenna, which maintained all the advantages of standard microstrip patch antennas, was achieved. It was noted that no loss in gain or perturbation of radiation pattern occurs for the broadband element. The theoretical design was shown to be close in its predictions, but empirical iteration is required to actually produce a working broadband element. This is to account for variables not included in the theoretical analysis.

SECTION V

SCALING FREQUENCY

Applications for the broadband element design of this paper can require operation at Ka or Millimeter wave bands as well as lower bands. A practical limit to the lowest frequency of use for the patch antenna will be at the point where the increased size of the patch becomes undesirable, making the antenna too large (around the VHF range). A limit on the maximum frequency for use is where dielectric losses and batch to batch dielectric drift make the antenna impractible. The introduction (Section I) pointed out that as of 1982, patch antennas had been used up to about 60 GHz. As substrate materials are improved, monolithic integrated circuit technology could yield patch antennas through Millimeter wave band. Testing and proving designs become more difficult at these higher frequencies. A method of scaling known working designs to new frequency ranges is desirable. If accurate scaling can be accomplished, it will allow building a conveniently scaled down element or array at a frequency convenient for testing (such as the X band frequencies used in this paper) and then scaling it up to the desired frequency once it is proven.

The variable groups in a microstrip patch antenna element design are: patch sizes, dielectric thicknesses and dielectric constants. It seems feasible

that if the number of wavelengths of both dielectric height and patch size are held constant over frequency, the operation of the element will be the same for all practical frequencies. Therefore, scaling of the variables of a known working element so that the wavelength dimensions are the same at another frequency should produce a working element at that frequency. The most inflexible of the variables for scaling is the dielectric constant. The surest way of scaling is to use the same upper and lower dielectric that is used in the known working element. Changing ϵ_r would require calculation of wavelength in the new effective dielectric of the microstrip, a term which is only approximately known. Leaving the dielectrics the same in the desired element as in the known good element will cause the effective dielectric term to cancel out of the ratios of patch length and dielectric height. Therefore, maintaining the dielectrics, the ratio of the known patch length to the new desired patch length, and the ratio of the known dielectric height to the new dielectric height will equal the ratio of the desired frequency to the known resonant frequency. As an example, to scale one of the X band two-layer designs of this paper to a center frequency of 35 GHz, the parameters of the desired element will be:

RATIO=(center frequency of known working element) / (35 GHz)

$$\epsilon_{rL_{new}}=\epsilon_{rL_{known}} \qquad \epsilon_{rU_{new}}=\epsilon_{rU_{known}}$$

$$h_{L_{new}}=h_{L_{known}} \times \text{RATIO} \qquad h_{U_{new}}=h_{U_{known}} \times \text{RATIO} \qquad (5\text{-}1)$$

$$L_{L_{new}}=L_{L_{known}} \times \text{RATIO} \qquad L_{U_{new}}=L_{U_{known}} \times \text{RATIO}$$

A problem of nonstandard dielectric heights resulting from equation 5-1 is apparent. One way to circumvent this problem is to iterate the X band design until a center frequency is obtained which yields standard substrate thicknesses for $h_{L_{new}}$ and $h_{U_{new}}$. A less exact, but practical method is to compare family curve data (Figure 17) of elements with different dielectric heights, all other parameters close to the same, and interpolate the result of an adjustment of the new dielectric heights to standard substrate thicknesses.

As yet, the author has not tested the above scaling method, but an initial test to prove its feasibility would be to try it so that all fixturing and testing remain the same between the the known and the scaled elements. This will eliminate other unknowns. The fixturing used for the experimental data of Section IV of this paper has an upper frequency limit, set by the SMA connector, of 25 GHz. Scaling the configuration of Figure 13(a) so that its upper band limit (around 10 GHz) is adjusted to 25 GHz would give new parameters of:

RATIO=10/25=.4

$\epsilon_{rL}=10.5$	$\epsilon_{rU}=2.2$
$h_{L_{new}}=.010''$	$h_{U_{new}}=.0368''$
$L_{L_{new}}=.200cm=.0787''$	$L_{U_{new}}=.334cm=.1315''$

The only problem dimension is $h_{U_{new}}$. The curves for the X band patch show that, all other parameters the same, broadbanding occurred for h_U=.092 (BW=24.9%) and h_U=.102 (BW=22.9%) with the upper patch resonance remaining about the same and the lower patch resonance changing 0.4 GHz. Therefore $h_{U_{new}}$ could be rounded up to .040″ without affecting broadband behavior. Note that the lower patch dimension, which is etched on a high dielectric, is getting quite small. For comparison, at 35 GHz $L_{L_{new}}$=.143cm=.0562″ and $L_{U_{new}}$=.239cm=.0940″. Tolerances in production of the patch elements must be scaled the same as the patch sizes.

In order to test a 35 GHz element, a new fixturing method must be used. The following are some suggestions for this fixture. The lower feed patch will probably be fabricated with a 50 Ω microstrip feed line extending out from the element an inch or so. There, a microstrip to waveguide connection can be made with a small coax or pin. The center coax conductor or pin will be extended, until matched, into the waveguide at a point a quarter wavelength from the shorted end of the waveguide [13], with the other end of the guide going to a Ka band source. The thin dielectric heights of the 35 GHz element will probably require that the elements be laminated with a thin adhesive prior to testing. Some shifting will occur from the adhesive.

SECTION VI

SUMMARY AND CONCLUSION

A broadband, contiguous stacked, two-layer, square microstrip patch antenna element design which can be used for linear or circular polarization was introduced. Single layer microstrip patch theory was modified for the two-layer element and predictions of the radiation pattern and resonant frequencies were made. Testing of the design was done at X band with linear polarization. Experimental results showed that the design produced a practical broadband microstrip antenna element which maintained all the advantages of standard microstrip patch antennas. No loss in gain or perturbation of radiation pattern occurred. It appears that conservation of misery was not enforced. Scaling techniques were described for obtaining parameters for a higher frequency element, such as for a center frequency of 35 GHz. Overall, the element design was a success and is ready for use in microstrip array antennas.

APPENDIX A

OTHER BROADBANDING METHODS

Other attempts at broadbanding microstrip antennas have been reported. Some of these are mentioned here along with some of their disadvantages.

- Kumar and Gupta [14] have achieved broadbanding with coupled resonators on the same plane. However, this produces a bulky element hard to use in array applications.

- Chang, Long and Richards [15] obtained bandwidths up to 20% with a single patch etched on an electrically thick, low dielectric substrate (up to $.23\lambda_d$ or about 0.136″ thick at 10 GHz). Radiation patterns were found very similar to the typical thin microstrip antenna. Impedances were characterized by a substantial inductive shift in reactance at resonance due to the feed passing through the thick substrate. In actual use, an additional reactive network for impedance matching would be required. The low dielectric is also not advantageous to some designs since it does not lend itself to integration with feed structures. The necessary substrate thickness may also be too great. Yasuo et al. [16] has also done work in this area obtaining bandwidths exceeding 10%.

- Saban [17] and Chen et al. [18] have done broadbanding work with two-layer stacked circular radiators. Both linear and circular polarizations were achieved with bandwidths up to 15% (2:1 VSWR) by Saban and more than 20% (1.92:1 VSWR) by Chen. However, both designs have the layers separated by an air gap. This yields a large element thickness, not advantages to some designs, as well as an element harder to manufacture and harder to launch-harden.

- Hall et al. [19] obtained bandwidths of 13% with two-layer stacked rectangular patch radiators. Only empirical work was done. Capacitive stubs had to be added to the feed line, making the element more complex. Also for matching, an empirical adjustment of the overlap of the two patches had to be performed, yielding a nonsymmetrical element.

APPENDIX B

MATERIAL SPECIFICATIONS

The following three pages are product data for Rogers Corporation's RT Duroid microwave substrate product. Similar materials are also available from Keene Corporation and 3M.

ROGERS

RT/duroid 5880

PROPERTY	TEST METHOD, CONDITION		UNITS[1]	DIRECTION	TYPICAL VALUE[2]	
Dielectric constant, εr	ASTM D1531	1 MHz	—	Z	2.20	
	ASTM D3380	10 GHz	—	Z	2.20 ± .02 spec.	
Dissipation factor, tan δ	ASTM D1531	1 MHz	—	Z	.0004	
	ASTM D3380	10 GHz	—	Z	.0009	
Volume resistivity	ASTM D257	C96/23/95	Mohm cm	Z	2×10^7	
Surface resistivity	ASTM D257	C96/23/95	Mohm	X,Y	3×10^8	
					Test at 23°C	Test at 100°C
Tensile modulus	ASTM D638	A	MPa (kpsi)	X	1070 (156)	450 (65)
				Y	860 (125)	380 (55)
ultimate stress			MPa (kpsi)	X	29 (4.2)	20 (2.9)
				Y	27 (3.9)	18 (2.6)
ultimate strain			%	X	6.0	7.2
				Y	4.9	5.8
Compressive modulus	ASTM D695	A	MPa (kpsi)	X	710 (103)	500 (73)
				Y	710 (103)	500 (75)
				Z	940 (136)	670 (97)
ultimate stress			MPa (kpsi)	X	27 (3.9)	22 (3.2)
				Y	28 (4.0)	21 (3.1)
				Z	52 (7.5)	43 (6.3)
ultimate strain			%	X	8.5	8.4
				Y	7.7	7.8
				Z	12.5	17.6
Deformation under load	ASTM D621				Test at 150°C	
		24 hr/14MPa(2 kpsi)	%	Z	1.0	
Water absorption	ASTM D570	D 24/23				
		Thickness = 0.8mm(.031 in)	mg (%)		0.9 (.02)	
		Thickness = 1.6mm(.062 in.)	mg (%)		1.3 (.015)	
Specific gravity	ASTM D792		—		2.2	
Heat distortion temperature	ASTM D648	1.82MPa(264 psi)	°C(°F)	X,Y	>260 (>500)	
Specific heat	Calculated		J/g/K(BTU/lb/°F)		0.96 (.23)	
Thermal conductivity	Rogers TR2721		W/m/K(BTU in/ft²/hr/°F)	Z	0.26 (1.8)	
Thermal expansion	ASTM D3386		mm/m	→	X	Y	Z
	(10 K/min.)	−100°C			−6.1	−8.7	−18.7
		15			−0.9	−1.8	− 6.9
(Values given are total change from a base temperature of 35°C)		25			−0.5	−0.9	− 4.5
		75			1.1	1.5	8.7
		150			2.3	3.2	28.3
		250			3.8	5.5	69.5

[1] SI units given first with other frequently used units in parentheses.

[2] From internal TR's 1430, 2224, 2854. Tests were at 23°C unless otherwise noted.

Printed in U.S.A.

Revised 3/81
Supersedes 1/78
8359-065-5.0-IL

ROGERS

RT/duroid 6010.5

PROPERTY	TEST METHOD, CONDITION		UNITS[1]	DIRECTION	TYPICAL VALUE [2]
Dielectric constant, ε_r	Adapted ASTM D3380, 10 GHz	A	—	Z	10.5 ± .25, spec.
Thermal coefficient of ε_r	Adapted ASTM D3380, 10 GHz	−50 to 170°C	ppm/°C	Z	−370
Dissipation factor, tan δ	Adapted ASTM D3380, 10 GHz	A	—	Z	.0028 max., spec.
Tensile modulus	ASTM D638 (0.1/min. strain rate)	A	MPa (kpsi)	X	931 (135)
				Y	559 (81)
ultimate stress		A	MPa (kpsi)	X	17 (2.4)
				Y	13 (1.9)
ultimate strain		A	%	X	9 to 15
				Y	7 to 14
Compression modulus	ASTM D695 (.05/min. strain rate)	A	MPa (kpsi)	Z	2144 (311)
ultimate stress			MPa (kpsi)	Z	47 (6.9)
ultimate strain			%	Z	25
Flexural modulus	ASTM D790	A	MPa (kpsi)	X	4364 (633)
				Y	3751 (544)
ultimate stress			MPa (kpsi)	X	36 (5.2)
				Y	32 (4.4)
Deformation under load	ASTM D621	24 hr/50°C/7MPa	%	Z	0.26
		24 hr/150°C/7MPa	%	Z	1.37
Water absorption	ASTM D570	24 hr/23°C, .050" thick.	%		0.1
		48 hr/50°C, .050" thick.	%		0.25
Specific gravity	ASTM D792	—	—		2.9
Specific heat	Calculated		J/g/K (BTU/lb/°F)		1.00 (.239)
Thermal conductivity	Rogers TR 2721	23 to 100°C	W/m/K (BTU in/ft²/hr/°F)	Z	0.41 (2.87)

Thermal expansion (5 K/min.) (Values given are total change from a base temperature of 35°C)		mm/m	–	X	Y	Z
	−100° C			−2.8	−3.0	−3.4
	− 50			−2.0	−2.1	−2.6
	10			−0.8	−0.8	−1.1
	75			1.0	1.0	0.7
	150			2.2	2.2	1.7
	250			3.7	3.8	4.3
	315			5.0	5.1	8.4

[1] SI units given first with other frequently used units in parentheses.

[2] References: APR 4022.44; DJS 4019-27-32; Internal TR 2610. Tests were at 23°C unless otherwise noted. Typical values should not be used for specification limits.

Printed in U.S.A.

Revised 2/86

Supersedes 3/83

9340-036-5.0-HG

ROGERS

RT/duroid® 6006

PROPERTY	TEST METHOD, CONDITION		UNITS [1]	DIRECTION	TYPICAL VALUE [2]
Dielectric constant, ϵ_r	Adapted ASTM D3380, 10 GHz	A	—	Z	6.00 ± .20, spec.
Dissipation factor, tanδ	Adapted ASTM D3380, 10 GHz	A	—	Z	.0027 max, spec.
Tensile modulus	ASTM D638 (0.1/min. strain rate)	A	MPa (kpsi)	X	510(740)
				Y	627(91)
ultimate stress		—	MPa (kpsi)	X	20(2.8)
				Y	17(2.5)
ultimate strain		—	%	X	12 to 13
				Y	4 to 6
Compression modulus	ASTM D695 (.05/min. strain rate)	A	MPa (kpsi)	Z	1069(155)
ultimate stress		—	MPa (kpsi)	Z	54(7.9)
ultimate strain		—	%	Z	33
Flexural modulus	ASTM D790	A	MPa (kpsi)	X	2634(382)
				Y	1951(283)
ultimate stress		—	MPa (kpsi)	X	43(6.3)
				Y	38(5.5)
Deformation under load	ASTM D621	24 hr/50°C/7MPa	%	Z	0.33
		24 hr/150°C/7MPa	%	Z	2.1
Water absorption	ASTM D570	24 hr/23°C, .050" thick	%		0.05
		48 hr/50°C, .050" thick	%		0.18
Specific gravity	ASTM D792	—	—		2.7
Specific heat	(Calculated)		J/g/K (BTU/lb./°F)		0.97(0.231)
Thermal conductivity	Rogers TR 3824 [3]	23 to 100° C	W/m/K (BTU in/ft²/hr/°F)	Z	0.48(3.3)

Thermal expansion (Values shown are total change from a base temperature of 35°C)	ASTM D3386	mm/m	X	Y	Z
		− 50° C	− 4.0		
		10	− 1.7	− 1.9	− 3.8
		75	1.2	1.3	1.9
		150	2.6	2.9	3.7
		250	4.7	5.4	8.7
		315	6.6	7.5	12.7

[1] S1 units given first with other frequently used units in parentheses.

[2] References: APR 4022:44; DJS 4019:27-32; Internal TR 2610. Tests were 23°C unless otherwise noted. Typical values should not be used for specification limits.

[3] Using the Colora Thermoconductometer.

Revised 2/86
Supercedes 5/85
9340-036-5.0-HG

APPENDIX C

LIST OF ELEMENTS WITH DIMENSIONS

	DIELECTRIC CONSTANT	DIELECTRIC HEIGHT (h)	SQUARE PATCH LENGTH SPECIFIED	MEASURED LENGTH (L)
LOWER FEED	2.2	.020"=.0508CM	.331"=.8406CM	.3295"=.837CM
LOWER FEED	6.0	.025"=.0635CM	.200"=.5080CM	.1984"=.504CM
LOWER FEED	6.0	.025"=.0635CM	.220"=.5588CM	.2173"=.552CM
LOWER FEED	6.0	.025"=.0635CM	.240"=.6096CM	.2382"=.605CM
LOWER FEED	6.0	.025"=.0635CM	.265"=.6731CM	.2618"=.665CM
LOWER FEED	6.0	.050"=.1270CM	.200"=.5080CM	.1969"=.500CM
LOWER FEED	10.5	.010"=.0254CM	.165"=.4191CM	.1634"=.415CM
LOWER FEED	10.5	.010"=.0254CM	.173"=.4394CM	.1713"=.435CM
LOWER FEED	10.5	.010"=.0254CM	.185"=.4699CM	.1831"=.465CM
LOWER FEED	10.5	.010"=.0254CM	.200"=.5080CM	.1961"=.498CM
LOWER FEED	10.5	.025"=.0635CM	.165"=.4191CM	.1642"=.417CM
LOWER FEED	10.5	.025"=.0635CM	.173"=.4394CM	.1713"=.435CM
LOWER FEED	10.5	.025"=.0635CM	.185"=.4699CM	.1835"=.466CM
LOWER FEED	10.5	.025"=.0635CM	.200"=.5080CM	.1969"=.500CM
UPPER ELEMENT	2.2	.010"=.0254CM	.331" =.8407CM	.3286"=.835CM
UPPER ELEMENT	2.2	.015"=.0381CM	.331" =.8407CM	.3299"=.838CM
UPPER ELEMENT	2.2	.020"=.0508CM	.23622"=.600CM	.2339"=.594CM
UPPER ELEMENT	2.2	.020"=.0508CM	.25590"=.650CM	.2535"=.644CM
UPPER ELEMENT	2.2	.020"=.0508CM	.27559"=.700CM	.2732"=.694CM
UPPER ELEMENT	2.2	.020"=.0508CM	.28543"=.725CM	.2827"=.718CM
UPPER ELEMENT	2.2	.020"=.0508CM	.30984"=.787CM	.3063"=.778CM
UPPER ELEMENT	2.2	.020"=.0508CM	.297" =.7544CM	.2953"=.750CM
UPPER ELEMENT	2.2	.020"=.0508CM	.322" =.8179CM	.3173"=.806CM
UPPER ELEMENT	2.2	.020"=.0508CM	.331" =.8407CM	.3291"=.836CM
UPPER ELEMENT	2.2	.020"=.0508CM	.386" =.9804CM	.3839"=.975CM
UPPER ELEMENT	2.2	.031"=.07874CM	.23622"=.600CM	.2331"=.592CM
UPPER ELEMENT	2.2	.031"=.07874CM	.25590"=.650CM	.2531"=.643CM
UPPER ELEMENT	2.2	.031"=.07874CM	.27559"=.700CM	.2728"=.693CM
UPPER ELEMENT	2.2	.031"=.07874CM	.28543"=.725CM	.2835"=.720CM
UPPER ELEMENT	2.2	.031"=.07874CM	.30984"=.787CM	.3075"=.781CM
UPPER ELEMENT	2.2	.031"=.07874CM	.297" =.7544CM	.2949"=.749CM
UPPER ELEMENT	2.2	.031"=.07874CM	.322" =.8179CM	.3201"=.813CM
UPPER ELEMENT	2.2	.031"=.07874CM	.331" =.8407CM	.3287"=.835CM
UPPER ELEMENT	2.2	.031"=.07874CM	.386" =.9804CM	.3839"=.975CM
UPPER ELEMENT	2.2	.031"=.07874CM	.430" =1.092CM	.4272"=1.085CM
UPPER ELEMENT	2.2	.062"=.15748CM	.23622"=.600CM	.2339"=.594CM
UPPER ELEMENT	2.2	.062"=.15748CM	.25590"=.650CM	
UPPER ELEMENT	2.2	.062"=.15748CM	.27559"=.700CM	.2740"=.696CM
UPPER ELEMENT	2.2	.062"=.15748CM	.28543"=.725CM	.2823"=.717CM
UPPER ELEMENT	2.2	.062"=.15748CM	.30984"=.787CM	.3075"=.781CM
UPPER ELEMENT	2.2	.062"=.15748CM	.297" =.7544CM	.2953"=.750CM
UPPER ELEMENT	2.2	.062"=.15748CM	.322" =.8179CM	.3193"=.811CM
UPPER ELEMENT	2.2	.062"=.15748CM	.331" =.8407CM	.3287"=.835CM
UPPER ELEMENT	2.2	.062"=.15748CM	.386" =.9804CM	.3815"=.969CM
UPPER ELEMENT	2.2	.062"=.15748CM	.430" =1.092CM	.4260"=1.082CM
UPPER ELEMENT	2.2	.125"=.3175CM	.331" =.8407CM	.3268"=.830CM

LIST OF REFERENCES

[1] Bahl, I. J., and Bhartia, P. Microstrip Antennas. Dedham, Massachusetts: Artech House, Inc., 1982.

[2] James, J. R.; Hall, P. S.; and Wood, C. Microstrip Antenna Theory and Design. London and New York: Peter Peregrinus Ltd. on behalf of the IEE, 1981.

[3] Carver, K. R., and Mink, J. W. "Microstrip Antenna Technology." IEEE Transactions on Antennas and Propagation AP-29 (January 1981): 2-24.

[4] Balanis, C. A. Antenna Theory Analysis and Design. New York: Harper and Row Publishers, Inc., 1982, pp. 487-496.

[5] Lo, Y. T.; Solomon, D.; and Richards, W. F. "Theory and Experiment on Microstrip Antennas." IEEE Transactions on Antennas and Propagation AP-27 (March 1979): 137-145.

[6] Sengupta, D. L. "The Transmission Line Model for Rectangular Microstrip Antennas." IEEE AP-S International Symposium Digest (1983): 158-161.

[7] Munson, R. E. "Microstrip Antennas." In Antenna Engineering Handbook, Chapter 7. Edited by R. C. Johnson, and H. Jasik. New York: McGraw Hill, 1984.

[8] Bailey, M. C., and Deshpande, M. D., "Analysis of Rectangular Microstrip Antennas." NASA Technical Paper 2276 (1984).

[9] Ramo, S.; Whinnery, J. R.; and Van Duzer, T. Fields and Waves in Communication Electronics. New York: John Wiley and Sons, 1984, pp. 491-492.

[10] Schneider, M. V. "Microstrip Lines for Microwave Integrated Circuits." The Bell System Technical Journal (May-June 1969): 1421-1444.

[11] Bahl, I. J.; Bhartia, P.; and Stuchly, S. S. "Design of Microstrip Antennas Covered with a Dielectric Layer." IEEE Transactions on Antennas and Propagation AP-30 (March 1982): 314-318.

[12] Oltman, G., and Huebner, D. A. "Electromagnetically Coupled Microstrip Dipoles." IEEE Transactions on Antennas and Propagation AP-29 (January 1981): 151-157.

[13] Weiss, M. A. "Microstrip Antennas for Millimeter Waves." IEEE Transactions on Antennas and Propagation AP-29 (January 1981): 171-174.

[14] Kumar, G., and Gupta, K. C. "Broadband Microstrip Antennas Using Coupled Resonators." IEEE AP-S International Symposium Digest (1983): 67-70.

[15] Chang, E.; Long, S. A.; and Richards, W. F. "An Experimental Investigation of Electrically Thick Rectangular Microstrip Antennas." IEEE Transactions on Antennas and Propagation AP-34 (June 1986): 767-772.

[16] Yasuo, S.; Miyano, N.; and Chiba, T. "Expanding The Frequency Bandwidth of a Microstrip Antenna." IEEE AP-S International Symposium Digest (1981): 366-369.

[17] Sabban, A. "A New Broadband Stacked Two-Layer Microstrip Antenna." IEEE AP-S International Symposium Digest (1983): 63-66.

[18] Chen, C. H.; Tulintseff, A.; and Sorbello, R. M. "Broadband Two Layer Microstrip Antenna." IEEE AP-S International Symposium Digest (1984): 251-254.

[19] Hall, P. S.; Wood, C.; and Garrett, C. "Wide Bandwidth Microstrip Antennas for Circuit Integration." Electronic Letters Volume 15 (1979): 458-459.